

## Durham E-Theses

---

### *Towards single-photon emission from zero-wave vector Rydberg polaritons in thermal caesium*

CHARMAN, ANTON

#### How to cite:

---

CHARMAN, ANTON (2022) *Towards single-photon emission from zero-wave vector Rydberg polaritons in thermal caesium*, Durham theses, Durham University. Available at Durham E-Theses Online:  
<http://etheses.dur.ac.uk/14785/>

#### Use policy

---

The full-text may be used and/or reproduced, and given to third parties in any format or medium, without prior permission or charge, for personal research or study, educational, or not-for-profit purposes provided that:

- a full bibliographic reference is made to the original source
- a [link](#) is made to the metadata record in Durham E-Theses
- the full-text is not changed in any way

The full-text must not be sold in any format or medium without the formal permission of the copyright holders.

Please consult the [full Durham E-Theses policy](#) for further details.

# Towards single-photon emission from zero-wave vector Rydberg polaritons in thermal caesium

Anton Charman

---

A thesis submitted in partial fulfilment  
of the requirements for the degree of  
Master of Science



Department of Physics  
Durham University

7th August 2022

# Towards single-photon emission from zero-wave vector Rydberg polaritons in thermal caesium

Anton Charman

---

## Abstract

This thesis presents the design, modelling and preliminary experimental setup of a deterministic single-photon emitter scheme. It relies on storing a three-beam zero-wave vector Rydberg polariton in a caesium thermal vapour through dressed-state electromagnetically induced transparency (EIT).

EIT was experimentally studied through  $6S_{1/2} \rightarrow 6P_{1/2} \rightarrow 6D_{3/2}$  in room temperature thermal caesium, and data was compared to an analytic model derived for weak probe velocity-averaged hyperfine absorption. Peak heights and widths were over-estimated because of a uniform intensity beam assumption and the lack of a strictly weak probe in the experiment. Along with fluorescence data from the  $7P_{1/2} \rightarrow 6S_{1/2}$  decay at 459.4 nm, EIT was shown to maximise the upper state population whilst simultaneously reducing the line centre probe absorption.

Dressed state three-level EIT is then derived from the four-level ladder Rydberg excitation scheme with laser parameters calculated for a  $2\pi \times 1$  GHz dressed state Autler-Townes splitting. The corresponding probe absorption was simulated for continuous wave and pulsed STIRAP excitation demonstrating expectedly weak Rydberg EIT. Polarisation spectroscopy was investigated for probe beam frequency stabilisation yielding a steep slope dispersive error signal. Finally, a bespoke hexagonal vapour cell was designed that minimises astigmatism aberrations from focusing beams across tilted planar interfaces. Dimensioned photographs of the fabricated cell display its readiness for use in future three-beam Doppler-free experiments.

# Declaration

I confirm that the work in this thesis is based on research carried out at the Quantum Light & Matter research group in Durham, England. No part of this thesis has been submitted elsewhere for any other degree or qualification.

Anton Charman, 07 Aug, 2022

The copyright of this thesis rests with the author. No quotation from it should be published without their prior written consent and information derived from it should be acknowledged.

# Acknowledgements

There are many people that I would like to thank. Firstly, within the Quantum Light & Matter subsection at Durham University: my supervisors Profs. Charles Adams and Kevin Weatherill, postdoctorate researchers Dani and Lucy, the mechanical and electronic workshop staff, my labmate Tom, my colleagues Max and Oliver, and the visiting students Annika and Karen. I am also extremely grateful to everyone else that I had conversations with regarding physics and other topics.

Within the city of Durham, I want to thank Luke for his friendship, hospitality and for sharing his general excitement for life. To Órfhlaith: I find myself lost for the words that best describe how you have enriched my life and supported me.

Outside of Durham, I want to acknowledge my friends from all over the world that have been a key part of my life. Finally, I am eternally indebted to my mother for the kindness and patience that she has shown me.

# Contents

<b>Abstract</b>	<b>i</b>
<b>Declaration</b>	<b>ii</b>
<b>Acknowledgements</b>	<b>iii</b>
<b>1 Introduction</b>	<b>1</b>
1.1 Single-photon sources . . . . .	3
1.2 Thermal vapours . . . . .	4
1.3 Thesis structure . . . . .	5
<b>2 EIT in ladder systems</b>	<b>6</b>
2.1 Theoretical background: two-level systems . . . . .	6
2.1.1 Atom-light interaction Hamiltonian . . . . .	6
2.1.2 Relaxation and the optical Bloch equations . . . . .	8
2.1.3 Macroscopic theory of absorption . . . . .	10
2.1.4 Weak probe regime optical response . . . . .	11
2.2 Three-level systems . . . . .	12
2.2.1 Dressed state interference . . . . .	12
2.2.2 Electromagnetically induced transparency . . . . .	14
2.3 Doppler broadening . . . . .	15
2.3.1 Two levels . . . . .	15
2.3.2 Three levels . . . . .	17

2.4	Multi-level theory . . . . .	18
2.4.1	Atomic structure . . . . .	18
2.4.2	Computing atomic properties . . . . .	20
2.5	The Cs D1 line - theory and experiment . . . . .	20
2.5.1	Theory . . . . .	20
2.5.2	Experiment . . . . .	22
2.6	Exciting $6S_{1/2} \rightarrow 6P_{1/2} \rightarrow 6D_{3/2}$ in caesium . . . . .	24
2.6.1	Theory . . . . .	24
2.6.2	Experiment . . . . .	27
2.7	Summary . . . . .	31
<b>3</b>	<b>Zero-wave vector Rydberg polaritons</b>	<b>32</b>
3.1	Introduction: single-photon storage scheme . . . . .	32
3.1.1	Dark-state polaritons . . . . .	33
3.1.2	The Rydberg blockade . . . . .	34
3.1.3	Uniform phase spin waves . . . . .	36
3.2	Doppler-free Rydberg excitation . . . . .	37
3.2.1	Excitation laser angles . . . . .	37
3.2.2	Dressed-state EIT . . . . .	39
3.2.3	STIRAP pulse timing diagram . . . . .	43
3.3	Custom Doppler-free cuvette . . . . .	44
3.3.1	Focal distortion across planar interfaces . . . . .	45
3.3.2	Cuvette design and fabrication . . . . .	46
3.3.3	Simulating transmission and velocity selection . . . . .	50
3.3.4	Knife edge probe beam waist data . . . . .	54
3.4	Future experimental layout . . . . .	56
3.4.1	Ground state polarisation spectroscopy data . . . . .	56
3.4.2	Probe beam amplitude EOM pulse data . . . . .	59
3.4.3	Experimental layout suggestions . . . . .	60

## CONTENTS

---

<b>4 Conclusion</b>	<b>62</b>
4.1 Summary of key results . . . . .	62
4.2 Outlook . . . . .	63
<b>A Data linearisation and normalisation</b>	<b>64</b>
<b>B Knife edge beam waist extraction</b>	<b>67</b>
<b>C Solving the optical Bloch equations</b>	<b>69</b>
<b>Bibliography</b>	<b>71</b>

# Chapter 1

## Introduction

This thesis presents the preliminary design, modelling and experimental setup of a deterministic single-photon emitter scheme based on a thermal vapour of caesium. Single-photon sources are key in realising quantum technologies where the fundamental quantum bit (qubit) is the photon. Such technologies would enable improved capabilities for metrology, computing [1, 2] and information processing [3], as well as investigating quantum optics phenomena [4, 5].

Quantum computers are of much interest to scientific and technical communities because of their very attractive and alarming potential applications. For instance, they put public key cryptography at risk because of the potential to implement Shor's algorithm for prime factor decomposition. There is also the potential to implement Grover's quantum search algorithm that yields polynomial time speed-ups, and to simulate quantum systems [6]. Indeed, quantum computers are predicted to outperform classical computers in a particular set of tasks, but cannot be considered a replacement technology [7].

One paradigm, the all-optical quantum computer, displays much potential for implementing quantum information processing. In 2001, a scheme for linear optics quantum computation was proposed that requires only single-photon sources, detectors and linear optical elements [8]. This scheme would suffer from weak photon-

photon interactions, which would affect scalability and put a heavy demand on resources. Successful systems would also require near-unity efficiency optical components and inherently inefficient storage/readout processes would need to be combated. However, developments in theory and experiment have reignited faith in realising a quantum computer via this paradigm [9]. For instance, introducing non-linearity in the system such as the Kerr effect through linear components would improve the issue of scalability.

The success of any future system will depend on our ability to integrate and interface technologies of different types and one promising platform that could couple single photons to different qubit technologies is the Rydberg polariton [10]. This is a light-matter excitation where a photon is stored as a collective excitation across an ensemble of atoms via electromagnetically induced transparency (EIT) [11]. Mapping photons to polaritons creates a very strong and long-range contactless photon-photon interaction [5], which further motivates the all-optical quantum computer. Since the stored photon's polaritonic wavefunction is comprised of the relative phases of atoms in the ensemble, atomic motion-induced dephasing will change the read-out photon mode. This dephasing can be countered by using cold atom platforms [12] though at the expense of bulky and complex experimental hardware.

Alternatively, a Doppler-free zero wave vector scheme would enable a stored Rydberg polariton to become robust to motion-induced dephasing. Preliminary work from Durham University in 2016 [13] demonstrated a three-step Doppler-free EIT scheme in a thermal vapour of caesium excited to  $|8P_{1/2}\rangle$ , which forms the basis for this research project. Overall, the aim is to extend the Doppler-free results from low-lying states of caesium in Ref. [13] to Rydberg levels in a caesium thermal vapour to make a deterministic Rydberg thermal vapour single-photon source.

## 1.1 Single-photon sources

There exist two main categories of single photon emitters [14]; deterministic sources based on single emitters [15–21], atomic ensembles [10, 22–24], and probabilistic (heralded) sources based on parametric downconversion [25] and four-wave mixing [26, 27]. The second-order intensity correlation function  $g^{(2)}(\tau)$  for the probability of multi- to single-photon emission, defines antibunching for zero time delay as  $g^{(2)}(0) = 0$  [28]. This metric, along with indistinguishable single-mode, on-demand emission, defines the ideal source. However, real sources undergo trade-offs and deviations from ideality.

For instance, cold atom systems are experimentally complex and have low overall emission efficiencies with reasonable single-photon character E.g. 2.4 % and  $g^{(2)}(0) = 0.06$  [15], but are identical and scalable emitters. Additionally, the heavily researched quantum dot [29] usually requires cryogenic operating temperatures and complex photon collection setups, but offers single-mode emission with recent work in Ref. [30] showing efficiencies of 57 % and  $g^{(2)}(0) = 0.02$ .

There is also a deterministic ensemble platform, which exploits the Rydberg blockade [31, 32] at sufficiently high atomic densities to heavily suppress the probability of exciting more than one atom within a mesoscopic blockade radius. The single excitation is then read out and converted to a photon, as demonstrated in ensembles of ultracold caesium atoms trapped in a 1D optical lattice [10] and in room-temperature rubidium vapour micro-cells [23, 24]. This latter platform quotes a 4 % generation efficiency and  $g^{(2)}(0) = 0.21$ , but is of particular practical interest due to being an on-demand, room-temperature and relatively low complexity source. Additionally, a Rydberg polariton was stored in a 220  $\mu\text{m}$  thick rubidium vapour cell using a pulsed four-wave mixing scheme with a storage lifetime of 1.2 ns in [33]. This forms a storage time lower bound that future schemes should seek to surpass, but these references further motivate thermal vapours as a platform for quantum optics.

## 1.2 Thermal vapours

This thesis is centred on a level scheme identified in caesium, which has a melting point of 28.5 °C and one stable isotope -  $^{133}\text{Cs}$ . Alkali metal thermal vapours are a key platform for investigating quantum optics due to their simplicity, relatively low cost and controllable gaseous phase number density,  $N$ . Vapours are contained in glass cuvettes known as vapour cells, which makes them mechanically robust and easy to include in optical setups. Cell dimensions are usually in the centimetre and millimetre ranges all the way down to the micro- and nanoscale [33, 34].

The vapour pressure,  $P_v$ , of a gas is the pressure it exerts on its condensed phase counterpart and the walls of a closed container [35]. It is valid when the two phases are in equilibrium in a closed system at a fixed temperature. The Antoine equation then aims to model the temperature dependence of  $P_v$  using empirically determined coefficients [36]. A simplified form of the equation for a liquid condensed phase rewritten in SI units from [37] is

$$\log_{10}(P_v) = \log_{10}(101325) + 4.165 - \frac{3830}{T}, \quad (1.1)$$

where  $T$  is in Kelvin and  $P_v$  is in Pascals. If the ideal gas law applies for a sufficiently dilute vapour where inter-atomic interactions can be neglected, the relation  $N/V = P_v/(k_B T)$  holds. Rearrangement then approximates the average inter-atomic spacing,  $d$ , from  $N$  atoms distributed through a volume  $V$  such that  $V \sim Nd^3$  giving  $d \sim (N/V)^{-1/3}$ . However, corrections have been suggested based on nearest-neighbour analysis where,  $d \approx K(N/V)^{-1/3}$  with  $K \approx 5/9$  [38]. Figure 1.1 plots  $N$  and  $d$  against  $T$  in Celsius, where  $N$  increases by a factor of  $1 \times 10^4$  between  $T = 30^\circ\text{C}$  and  $200^\circ\text{C}$ . These relations demonstrate the controllability of the number density in thermal vapours.

Thermal vapours also introduce motional dephasing from nonzero sample temperatures resulting in broadenings from transit times across beam foci and inhom-

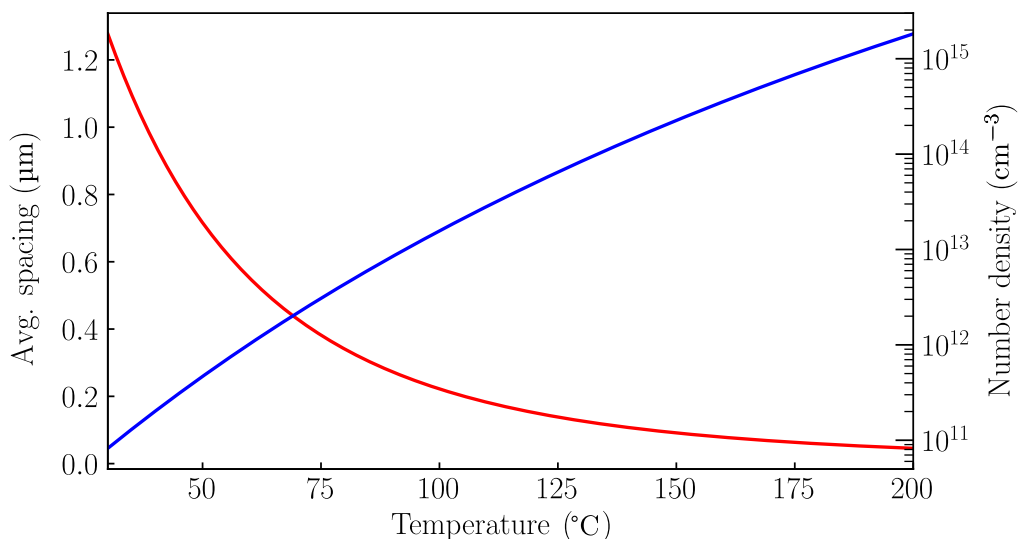


Figure 1.1: Plotting the number density (blue) and the average interatomic spacing (red) of caesium against temperature in celsius.

geneous Doppler broadening as well as velocity selection. The single-photon emitter scheme in this thesis relies on setting up a micrometre-scale Rydberg blockade volume [31], but atomic motion would smear out the phase distribution of the stored Rydberg polariton [13]. It is a Doppler-free arrangement of three incident beams that would make the scheme insensitive to such motion provided the zero-wave vector sum is perfect.

### 1.3 Thesis structure

The content in this thesis follows from the motivation of having a deterministic Rydberg caesium thermal vapour single photon source. Chapter two builds a model of atom-light interactions under the dipole approximation and introduces coherent phenomena arising from quantum interference in three or more level systems. Chapter three then presents the calculations for designing the three-beam Doppler-free scheme as well as preliminary simulations and experimental work. Finally, the conclusion summarises the key results of this work and gives an outlook for the next stages of this project.

# Chapter 2

## EIT in ladder systems

This chapter introduces the semi-classical theory of atom-light interactions by solving two-level atom dynamics. The developed formalism is then applied to three level systems where coherent electromagnetically induced transparency (EIT) is analysed. Extensions to multi-level theory are made to model hyperfine manifolds within the two- and three-level systems and finally, the models are compared with one- and two-photon experimental data in a caesium thermal vapour.

### 2.1 Theoretical background: two-level systems

#### 2.1.1 Atom-light interaction Hamiltonian

Consider a classical, monochromatic electromagnetic field incident on an isolated quantum mechanical two-level atom with ground and excited states coupled by a dipole-allowed transition [39]. The ground and excited states with eigenkets  $|1\rangle, |2\rangle$  have eigenenergies  $\hbar\omega_1, \hbar\omega_2$  and spontaneous decay rates  $\Gamma_1 = 0, \Gamma_2 = \Gamma$ , as depicted in Fig. 2.1. State  $|1\rangle$  represents a meta-stable ground state thereby having a zero natural decay. The incident radiation of angular frequency  $\omega$  is also detuned from the resonance frequency  $\omega_0 = \omega_2 - \omega_1$  by an amount  $\Delta = \omega - \omega_0$ . The beam's Rabi frequency is denoted by  $\Omega$ .

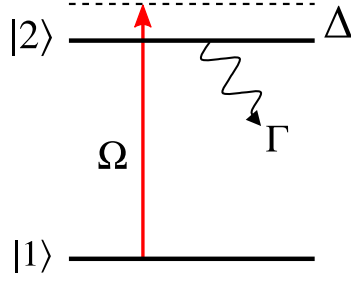


Figure 2.1: An isolated two-level atom level diagram with eigenkets  $|1\rangle, |2\rangle$  and spontaneous decay rates  $\Gamma_1 = 0, \Gamma_2 = \Gamma$ . The incident beam with Rabi frequency  $\Omega$  is detuned from resonance by  $\Delta = \omega - \omega_0$ .

For alkali metals with one outer electron, the electric field at the electron with position vector  $\mathbf{r}$  is given by

$$\mathcal{E}(\mathbf{r}, t) = \frac{1}{2} (\mathcal{E}_0 e^{i(\mathbf{k}\cdot\mathbf{r} - \omega t)} + \text{c.c.}) , \quad (2.1)$$

where  $\mathcal{E}_0$  and  $\mathbf{k}$  are the field strength and wavevectors. Since optical transition wavelengths are generally much larger than typical atomic sizes, the expansion  $e^{i\mathbf{k}\cdot\mathbf{r}} = 1 + i\mathbf{k}\cdot\mathbf{r} + \dots$  reduces to unity. This is the dipole approximation [40], where the quantum mechanical atom-light interaction Hamiltonian is

$$\hat{H}_1 = -\hat{\mathbf{d}} \cdot \hat{\mathcal{E}}(t) , \quad (2.2)$$

and the electric dipole moment operator is  $\hat{\mathbf{d}} = -e\hat{\mathbf{r}}$ , which is written using raising ( $|2\rangle\langle 1|$ ) and lowering ( $|1\rangle\langle 2|$ ) operators as  $\hat{\mathbf{d}} = d_{21}|2\rangle\langle 1| + d_{21}^*|1\rangle\langle 2|$  with a dipole matrix element  $d_{21} = \langle 2|\hat{\mathbf{d}}\cdot\hat{\mathbf{e}}|1\rangle$  [41]. Together with the bare atom Hamiltonian  $\hat{H}_0$ , the total system Hamiltonian is  $\hat{H} = \hat{H}_0 + \hat{H}_1$  and its wavefunction  $|\psi\rangle$  evolves according to the time-dependent Schrödinger equation  $i\hbar\partial_t|\psi\rangle = \hat{H}|\psi\rangle$ . Note that the matrix element of the transition  $|n\rangle \rightarrow |n'\rangle$  given  $\hat{H}$  is

$$\langle n|\hat{H}|n'\rangle = E_n\delta_{nn'} + \mathcal{E}\langle n|\hat{\mathbf{d}}\cdot\hat{\mathbf{e}}|n'\rangle \cos\omega t , \quad (2.3)$$

with eigenenergies  $E_n$  and  $\delta_{nn'}$  is the Kronecker delta. The field strength and po-

larisation unit vector are  $\mathcal{E}$  and  $\hat{\mathbf{e}}$ , respectively. The Rabi frequency  $\Omega_{nn'}$  for this transition is then defined to be

$$\hbar\Omega_{nn'} = \mathcal{E} \langle n | \hat{\mathbf{d}} \cdot \hat{\mathbf{e}} | n' \rangle . \quad (2.4)$$

Since transitions are between bound states the dipole matrix element  $\langle n | \hat{\mathbf{d}} \cdot \hat{\mathbf{e}} | n' \rangle$  and its Rabi frequency  $\Omega_{nn'}^* = \Omega_{n'n}$  will be real.

When expanding the interaction operator  $-\hat{\mathbf{d}} \cdot \hat{\mathcal{E}}(t)$ , the resulting terms will have  $e^{\pm i\omega t}$  prefactors [42]. Here, the rotating wave approximation (RWA) is applied to simplify analysis [43] by finding a unitary operator that transforms the system into a representation where rapidly oscillating components are neglected. The RWA violates the second law of thermodynamics [44], but the wealth of available quantum optics literature worldwide shows that it is an empirically justifiable approximation. Denoting the transformed quantities with a tilde and writing  $\Omega_{21} = \Omega_{12} = \Omega$  results in a matrix representation RWA system Hamiltonian of

$$\tilde{H} = \frac{\hbar}{2} \begin{pmatrix} 0 & \Omega \\ \Omega & -2\Delta \end{pmatrix} . \quad (2.5)$$

### 2.1.2 Relaxation and the optical Bloch equations

Introduced next is the density matrix formalism, which models processes that can't be included using the Hamiltonian - namely spontaneous emission. The density matrix is defined as  $\hat{\rho} = |\psi\rangle \langle\psi|$  and its equation of motion is the Liouville equation [45], which in the laboratory frame is  $d\hat{\rho}/dt = -i[\hat{H}, \hat{\rho}]/\hbar$ .

A general state ket  $|\psi\rangle$  is a probability amplitude  $c_i$  weighted superposition of basis states  $\{|i\rangle\}$ , so the density matrix elements are  $\rho_{ij} = c_i c_j^*$ . Diagonal elements represent population fractions and off-diagonal elements are coherences between the levels and are complex quantities. Applying the RWA to the Liouville equation allows rotating frame matrix elements  $\tilde{\rho}_{ij}$  to be considered, where populations are

unchanged by the transformation and so are written without tildes.

To model relaxation, a phenomenological spontaneous decay operator  $\hat{\mathcal{L}}$  is added to the Liouville equation to give the Lindblad master equation [46]

$$\frac{d\hat{\rho}}{dt} = -\frac{i}{\hbar}[\hat{H}, \hat{\rho}] + \hat{\mathcal{L}} . \quad (2.6)$$

Diagonal matrix elements  $\mathcal{L}_{ii}$  quantify the net population transfer into an atomic level  $|i\rangle$  due to spontaneous emission, which sets  $\text{Tr}(\mathcal{L}) = 0$ . Off-diagonal elements represent decays of coherences between the atomic levels  $|i\rangle$  and  $|j\rangle$  [41] as

$$\mathcal{L}_{ij} = -\frac{(\Gamma_i + \Gamma_j)\tilde{\rho}_{ij}}{2} . \quad (2.7)$$

For a ground state with  $\Gamma_1 = 0$  and an excited state  $\Gamma_2 = \Gamma$  the two-level decay matrix becomes

$$\mathcal{L} = \frac{1}{2} \begin{pmatrix} 2\Gamma\rho_{22} & -\Gamma\tilde{\rho}_{12} \\ -\Gamma\tilde{\rho}_{21} & -2\Gamma\rho_{22} \end{pmatrix} . \quad (2.8)$$

The Lindblad master equation then gives a set of coupled differential equations known as the optical Bloch equations. For two levels, these are

$$\frac{d\rho_{11}}{dt} = \frac{i\Omega}{2}(\tilde{\rho}_{12} - \tilde{\rho}_{21}) + \Gamma\rho_{22} , \quad (2.9a)$$

$$\frac{d\tilde{\rho}_{12}}{dt} = \frac{i\Omega}{2}(\rho_{11} - \rho_{22}) - \tilde{\rho}_{12} \left( \frac{\Gamma}{2} + i\Delta \right) , \quad (2.9b)$$

$$\frac{d\tilde{\rho}_{21}}{dt} = \frac{i\Omega}{2}(\rho_{22} - \rho_{11}) - \tilde{\rho}_{21} \left( \frac{\Gamma}{2} - i\Delta \right) , \quad (2.9c)$$

$$\frac{d\rho_{22}}{dt} = -\frac{d\rho_{11}}{dt} . \quad (2.9d)$$

A linear algebra solution to the optical Bloch equations is given in Appendix C, where the density matrix is reshaped to a column vector and the system of equations is re-cast as a matrix problem.

### 2.1.3 Macroscopic theory of absorption

The absorptive properties of a medium can be calculated by linking the macroscopic theory of linear dielectrics and the microscopic atomic dipole moment. Linear optics relates the applied time-dependent field and the electric polarisation  $P$  by using the complex susceptibility  $\chi$  as

$$P(t) = \frac{\epsilon_0}{2} (\chi \mathcal{E}_0 e^{-i\omega t} + \text{c.c.}) . \quad (2.10)$$

For an ensemble of atoms with number density  $N$ , the polarisation can also be related to the average dipole moment per unit volume  $\langle d \rangle$  through  $P(t) = N \langle d \rangle$  [47]. Using the wavefunction for a two-level system  $|\psi\rangle = c_1 |1\rangle + c_2 |2\rangle$  the expectation value becomes  $\langle d \rangle = -(d_{21} \rho_{21} + \text{c.c.})$  with  $d_{21} = \langle 2 | \hat{\mathbf{d}} \cdot \hat{\mathbf{e}} | 1 \rangle$ . Finally, using the rotating wave approximation to write  $\rho_{21} = \tilde{\rho}_{21} e^{-i\omega t}$  and comparing terms with Eq. 2.10 results in an expression for the susceptibility as

$$\chi = -\frac{2Nd_{21}^2}{\hbar\epsilon_0\Omega} \tilde{\rho}_{21} . \quad (2.11)$$

The complex refractive index of the medium is then  $n = \sqrt{1 + \chi}$ . For a monochromatic electric field with a free-space wavenumber  $k = \omega/c$  propagating a distance  $z$  through a medium with an isotropic complex refractive index  $n = n_R + in_I$ , the Beer-Lambert absorption coefficient is  $\alpha = 2\omega n_I/c$  [48], where  $\mathcal{T} = e^{-\alpha z}$ .

Dilute thermal vapours have small number densities and therefore small susceptibilities, so binomially expanding the refractive index yields  $n \approx 1 + \chi/2$  and therefore  $\alpha \approx \omega \chi_I/c$ . In quantum optics experiments the transition frequencies  $\omega_0/(2\pi)$  are typically hundreds of terahertz and detunings  $\Delta/(2\pi)$  are around tens of gigahertz, so  $\omega_0 \gg \Delta$  and the absorption coefficient can further be approximated as  $\alpha \approx \omega_0 \chi_I/c$  to give

$$\alpha = -\frac{2\omega_0 N d_{21}}{c\epsilon_0 \mathcal{E}} \text{Im}\{\tilde{\rho}_{21}\} . \quad (2.12)$$

### 2.1.4 Weak probe regime optical response

For a weak incident field such that  $\Omega \ll \Gamma$ , the ground state population remains mostly unperturbed such that  $\rho_{11} \approx 1$  and  $\rho_{22} \approx 0$ . Thereafter, solving the steady-state weak probe solution to Eq. 2.9b yields

$$\tilde{\rho}_{21}(\Delta) = -\frac{i\Omega}{\Gamma - 2i\Delta} . \quad (2.13)$$

Figure 2.2 shows the weak probe real dispersive and imaginary Lorentzian absorptive components of susceptibility. Strong probes saturate the excited state population, which monotonically reduces the line centre absorption [49].

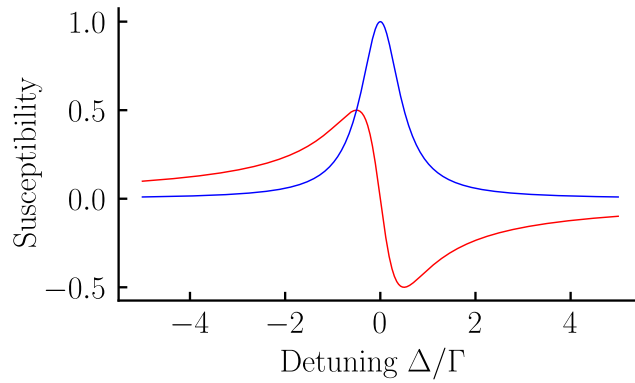


Figure 2.2: Two-level atom weak probe normalised susceptibility. Imaginary (blue) and real (red) components plotted against normalised detuning.

The weak probe power is estimated here for a linearly polarised collimated Gaussian beam with a peak intensity  $I_0$ ,  $1/e^2$  waists  $w_{x,y}$  in the  $x$ - $y$  plane and a total power of  $P = \pi w_x w_y I_0 / 2$  [50]. For a two-level transition, the on-resonance saturation intensity [37] for linearly polarised light is

$$I_{\text{sat}} = \frac{\hbar\omega_0^3\Gamma}{4\pi c^2} , \quad (2.14)$$

which for the caesium  $D_1$  transition is  $I_{\text{sat}} \approx 25.06 \text{ Wm}^{-2}$ . To mitigate the line centre absorption reduction from self- and hyperfine pumping the weak probe beam must satisfy  $I_0 \ll I_{\text{sat}}$ . For beams with FWHM radii of a few millimetres, ratios of

$I_0/I_{\text{sat}} = 10^{-3}$  to  $10^{-2}$  are sufficient to ensure the weak probe condition [49]. Larger beams result in larger times of flight for atoms moving through the beam, which requires a smaller  $I_0$  to ensure a weak probe.

## 2.2 Three-level systems

Two-level dynamics from the previous section are now extended to three-levels where the presence of two laser fields causes coherent phenomena to arise. In this thesis, the effect of interest is the reduction of the line centre absorption in the first-step beam when a much stronger and resonant second beam is present. This is known as electromagnetically induced transparency (EIT), which arises due to quantum interference between different excitation pathways in atomic level schemes [51–53].

### 2.2.1 Dressed state interference

Figure 2.3 shows the isolated three-level ladder scheme considered in this section. It has an eigenket basis  $\{|1\rangle, |2\rangle, |3\rangle\}$  with eigenenergies  $\hbar\omega_1 < \hbar\omega_2 < \hbar\omega_3$  and the levels have natural decay rates  $\Gamma_1 = 0, \Gamma_2 \neq \Gamma_3 \neq 0$ . The first-step ‘probe’ beam couples the ground and first excited states  $|1\rangle$  and  $|2\rangle$  with a resonance frequency  $\omega_{01}$ , a detuning  $\Delta_1 = \omega_1 - \omega_{01}$  and a Rabi frequency  $\Omega_1$ . The probe beam gains its name because it is detected on photodiodes in experiments to probe and measure the absorptive properties of the medium. The second ‘coupling’ beam couples the excited states  $|2\rangle$  and  $|3\rangle$  with a detuning  $\Delta_2 = \omega_2 - \omega_{02}$  and a Rabi frequency  $\Omega_2$ .

The RWA analysis from the two-level scheme can be applied to here to give the rotating frame three-level ladder Hamiltonian

$$\tilde{H} = \frac{\hbar}{2} \begin{pmatrix} 0 & \Omega_1 & 0 \\ \Omega_1 & -2\Delta_1 & \Omega_2 \\ 0 & \Omega_2 & -2(\Delta_1 + \Delta_2) \end{pmatrix}, \quad (2.15)$$

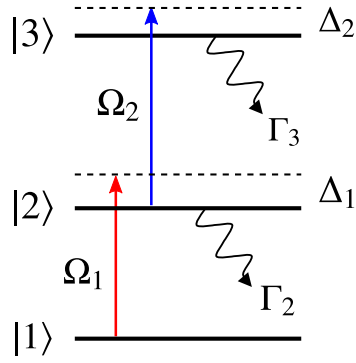


Figure 2.3: An isolated three-level atom level with eigenkets  $|1\rangle$ ,  $|2\rangle$ ,  $|3\rangle$  and nonzero spontaneous decay rates  $\Gamma_2, \Gamma_3$ . The probe beam and coupling beams have detunings and Rabi frequencies  $\Delta_1, \Omega_1$  and  $\Delta_2, \Omega_2$ , respectively.

where the new ‘dressed’ eigenkets in the presence of a second coupling laser are no longer the bare states  $\{|1\rangle, |2\rangle, |3\rangle\}$ . Consider the case of two-photon resonance ( $\Delta_1 + \Delta_2 = 0$ ). Diagonalising the Hamiltonian gives one eigenenergy as zero with an eigenket  $|v_0\rangle$  and two nonzero eigenenergies  $E_{\pm}$  with eigenkets  $|v_{\pm}\rangle$  [54] as

$$|v_+\rangle = \sin \theta \cos \phi |1\rangle + \sin \phi |2\rangle + \cos \theta \cos \phi |3\rangle , \quad (2.16a)$$

$$|v_-\rangle = \sin \theta \cos \phi |1\rangle - \sin \phi |2\rangle + \cos \theta \cos \phi |3\rangle , \quad (2.16b)$$

$$|v_0\rangle = \cos \theta |1\rangle - \sin \theta |3\rangle , \quad (2.16c)$$

and are parameterised using the following mixing angles

$$\tan \theta = \frac{\Omega_1}{\Omega_2} , \quad (2.17a)$$

$$\tan 2\phi = \frac{\sqrt{\Omega_1^2 + \Omega_2^2}}{\Delta_1} . \quad (2.17b)$$

State  $|v_0\rangle$  is a dark state because its zero eigenenergy means that atoms prepared in  $|v_0\rangle$  cannot be excited to another level. In the weak probe limit with  $\Delta_1 = \Delta_2 = 0$ , the new dressed states tend towards  $|v_0\rangle \rightarrow |1\rangle$  and  $|v_{\pm}\rangle \rightarrow (|2\rangle \pm |3\rangle)/\sqrt{2}$ . Therefore, excitation out of the dark state cannot occur even for an on-resonant weak probe when the second coupling laser is present and two-photon resonance is satisfied. This increased resonant probe transparency is electromagnetically induced transparency.

### 2.2.2 Electromagnetically induced transparency

By solving the optical Bloch equations (OBEs), the sensitivity of system parameters on EIT can be investigated. Following the rules for constructing  $\hat{\mathcal{L}}$  from the previous section, the phenomenological decay matrix for the ladder system in Fig. 2.3 is

$$\mathcal{L} = \frac{1}{2} \begin{pmatrix} 2\Gamma\rho_{22} & -\Gamma_2\tilde{\rho}_{12} & -\Gamma_3\tilde{\rho}_{13} \\ -\Gamma_2\tilde{\rho}_{21} & 2\Gamma_3\rho_{33} - 2\Gamma\rho_{22} & -(\Gamma_2 + \Gamma_3)\tilde{\rho}_{23} \\ -\Gamma_3\tilde{\rho}_{31} & -(\Gamma_2 + \Gamma_3)\tilde{\rho}_{32} & -2\Gamma_3\rho_{33} \end{pmatrix}. \quad (2.18)$$

Inserting the Hamiltonian and decay matrix into the Lindblad master equation in Eq. 2.6 then returns the OBEs for this system. In the weak probe limit where  $\rho_{11} \approx 1$  and  $\rho_{22} \approx \rho_{33} \approx 0$ , the steady-state coherence is [55]

$$\tilde{\rho}_{21}(\Delta_1, \Delta_2) = \frac{-i\Omega_1}{\Gamma_2 - 2i\Delta_1 + \frac{\Omega_2^2}{\Gamma_3 - 2i(\Delta_1 + \Delta_2)}}. \quad (2.19)$$

From Eq. 2.11,  $\chi$  is independent of  $\Omega_1$  because  $\chi \propto \tilde{\rho}_{21}/\Omega_1$ . Initially, the case of a detuned probe and resonant coupling beam with a varying Rabi frequency is investigated. The normalised line centre susceptibility denoted  $\chi/\chi_0$  reads

$$\frac{\chi}{\chi_0}(\Delta_1 = \Delta_2 = 0) = \frac{i\Gamma_3/\Gamma_2}{\Gamma_3/\Gamma_2 + (\Omega_2/\Gamma_2)^2}. \quad (2.20)$$

At one- and two-photon resonance, the real component  $\chi_R/\chi_0$  is always zero. When the condition  $\Omega_2/\Gamma_2 \gg \sqrt{\Gamma_3/\Gamma_2}$  is satisfied, the imaginary component  $\chi_I/\chi_0$  tends to zero, which shows the EIT line centre probe absorption reduction. Smaller values of  $\Gamma_3$  make it easier to observe EIT given a fixed  $\Omega_2$ .

Figure 2.4 shows the imaginary (blue) and real (red) components of the normalised weak probe susceptibility against detuning for  $\Delta_2 = 0$  with  $\Gamma_3/\Gamma_2 = 0.01$  for  $\Omega_2/\Gamma_2 = 0, 0.5, \text{ and } 2$ . For  $\Omega_2 = 0$  the lineshape is the two-level Lorentzian and the small  $\Gamma_3/\Gamma_2$  ratio makes the onset of EIT easily visible at a critical  $\Omega_2$ . The

transparency window broadens leaving two new absorption peaks whose separation increases with  $\Omega_2$ . This phenomenon is Autler-Townes splitting and is difficult to objectively separate from EIT [56]. The absorption lineshape doublet of states originates from the separation of the dressed state eigenenergies with  $\Omega_2$  [54].

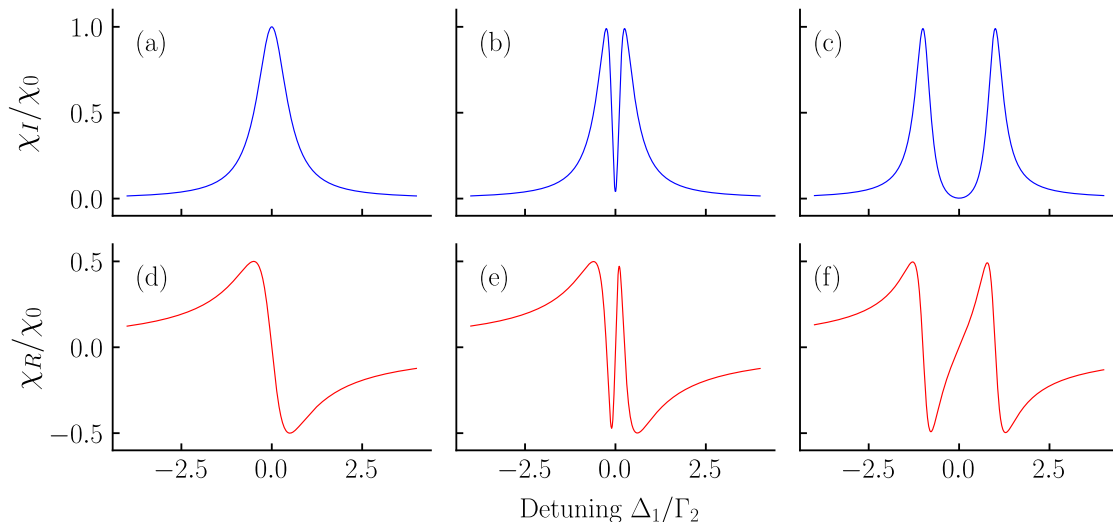


Figure 2.4: Three-level atom weak probe normalised susceptibility. Imaginary (blue) and real (red) components plotted against the normalised probe detuning with  $\Delta_2 = 0$  and  $\Gamma_3/\Gamma_2 = 0.01$ .

## 2.3 Doppler broadening

This thesis considers thermal vapours where atomic motion alters the perceived angular frequency of light,  $\omega'$ . For a beam with a wavevector  $\mathbf{k}$  the first-order shift is  $\omega' = \omega - \mathbf{k} \cdot \mathbf{v}$  [42], so only atoms with a component of velocity parallel to  $\mathbf{k}$  experience a Doppler shift.

### 2.3.1 Two levels

For a two-level (one-beam) system the corresponding 1D Maxwell-Boltzmann velocity distribution [57] denoted here as  $f_g(v)$  with ‘g’ for Gaussian is

$$f_g(v) = \frac{1}{u\sqrt{\pi}} e^{-\frac{v^2}{u^2}}, \quad (2.21)$$

where  $u = \sqrt{2k_B T/m}$  is the most probable speed for an atom of mass  $m$  at an absolute temperature  $T$ . The Doppler shift is included in the previous analysis by replacing  $\Delta$  with  $\Delta - kv$ , where  $v$  is the component of velocity along  $\mathbf{k}$ . The velocity-averaged susceptibility then accounts for contributions from all velocity classes as

$$\chi_I(\Delta) = \int \chi_I(\Delta, v) f_g(v) dv . \quad (2.22)$$

For stationary ultra cold atoms the lineshape of  $\chi_I$  is a Lorentzian with a natural linewidth  $\Gamma$ . However, as temperature increases the Gaussian Doppler width  $\Gamma_D = (\omega_0/c)\sqrt{k_B T/m}$  becomes significant and the integral of the Lorentzian and Gaussian in Eq. 2.22 produces the Voigt profile [58].

To understand the velocity dependence of the overall two-level susceptibility the imaginary normalised coherence  $\text{Im}\{\tilde{\rho}_{21}(\Delta, v)\}$  is plotted as a colour map in Figs. 2.5(a), (b) and (c) and the velocity-averaged coherence is plotted below in panels (d), (e) and (f). The nondimensional detuning  $\Delta' = \Delta/\Gamma$ , velocity  $v' = v/u$  and temperature  $a = ku/\Gamma$  are used, where  $a = 0, 0.5$  and  $2$  from left to right.

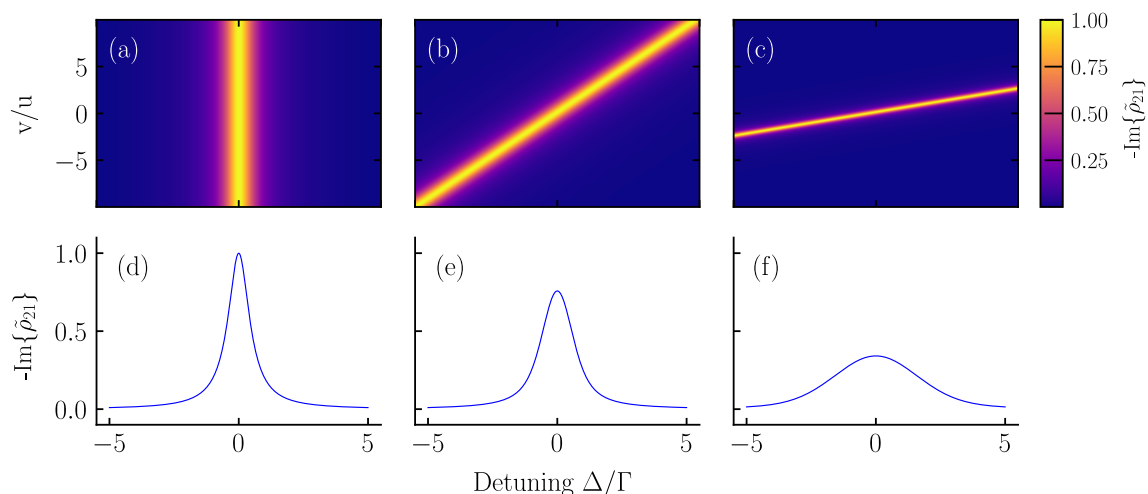


Figure 2.5: (a) to (c) show the velocity and detuning dependence of the normalised imaginary coherence and (d) to (f) are the corresponding Doppler-averaged coherences against detuning. The temperature-dependent parameter  $a = ku/\Gamma$  is  $a = 0, 0.5$  and  $2$  from left to right.

Figure 2.5 shows that for increasing temperatures the velocities that contribute significantly to  $\text{Im}\{\tilde{\rho}_{21}\}$  follow the slope  $1/a = \Gamma/(ku)$ . Furthermore, at a fixed detuning, the range of velocities that interact strongly with the probe beam decreases. This velocity selection leads to a lowered line centre Doppler-averaged coherence.

### 2.3.2 Three levels

To investigate EIT, assume a resonant coupling beam ( $\Delta_2 = 0$ ). The induced transparency is stronger when the residual Doppler broadening from  $-(\mathbf{k}_1 + \mathbf{k}_2) \cdot \mathbf{v}$  is reduced [55]. Since the majority of EIT experiments have  $\lambda_1 > \lambda_2$  [59], then a counter-propagating probe and coupling beam minimise the residual width through  $-(\mathbf{k}_1 + \mathbf{k}_2) \cdot \mathbf{v} = -(k_1 - k_2)v$ . The normalised counter-propagating coherence is then plotted as a colour map against the nondimensional probe detuning  $\Delta_1/\Gamma_2$  and velocity  $v/u$  in Figs. 2.6(a) to (c) with  $\lambda_1/\lambda_2 = 0.5, 1, 1.5$  from left to right. The corresponding velocity-averaged coherences are given in (d) to (f). The ratio of decays  $\Gamma_3/\Gamma_2 = 0.01$  is set to enlarge EIT features with  $\Omega_2/\Gamma_2 = 1$  and the nondimensional temperature is  $k_1u/\Gamma_2 = 1.5$ .

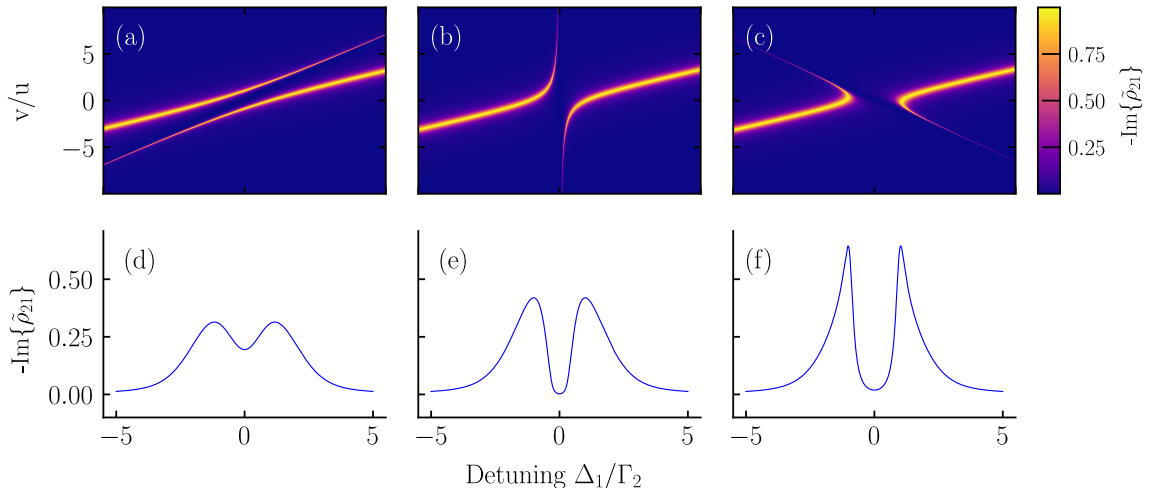


Figure 2.6: (a) to (c) show the velocity and detuning dependence of the normalised imaginary coherence and (d) to (f) are the corresponding Doppler-averaged coherences against detuning. The wavelength mismatch is varied as  $\lambda_1/\lambda_2 = 0.5, 1$  and  $1.5$  from left to right.

The colour maps in (a) to (c) demonstrate the nonzero probability of atoms existing whose Doppler shifts will give two-photon absorption to the upper state. This is represented by the thinner and darker peak coherence tails that follow the gradient  $\Gamma_2/(u(k_1 - k_2))$ , which is positive in (a), vertical in (b) where  $\lambda_1 = \lambda_2$  and negative in (c). The thinner tails show how the dressed states tend towards the initial eigenstates for large detunings and the thicker, brighter sections correspond to the one-photon resonance velocities where the gradient  $\Gamma_2/(k_1 u)$  is set by the temperature. From Figs. 2.6(d) to (f), EIT is suppressed when  $\lambda_1/\lambda_2 < 1$ . This occurs because for counter-propagating beams the Doppler shifts  $-k_1 v$  and  $-(k_1 - k_2)v$  have the same sign, which suppresses the line centre transparency window [59]. As the ratio increases the line centre coherence tends to zero thereby recovering EIT.

## 2.4 Multi-level theory

Real-world atomic systems differ from idealised two- and three-level models. This thesis is centred on caesium - an alkali metal with one valence electron, and this section briefly describes its atomic structure by summarising content from Ref. [60].

### 2.4.1 Atomic structure

The solution of the Schrödinger equation in a Coulomb potential gives the gross energy structure for hydrogen and the hydrogenic alkali metals. Levels are labelled with the principal and orbital angular momentum quantum numbers  $n$  and  $L$ .

A relativistic correction to the Schrödinger solution considers the spin of the electron  $\mathbf{S}$ . The electron orbital angular momentum  $\mathbf{L}$  couples to  $\mathbf{S}$  causing a spin-orbit interaction and leads to fine structure splitting. The total angular momentum  $\mathbf{J} = \mathbf{L} + \mathbf{S}$  with quantum number  $J$  satisfying  $|L - S| \leq J \leq |L + S|$  and a quantisation axis projection  $m_J$  describes the new eigenstates using the  $|n, L, S, J, m_J\rangle$  basis.

The electron's angular momentum  $\mathbf{J}$  then couples to the nuclear spin  $\mathbf{I}$  giving

hyperfine splitting that is smaller than the electronic energy scales. New eigenstates with total angular momentum  $\mathbf{F} = \mathbf{I} + \mathbf{J}$ , a quantum number  $F$  lying within the range  $|I - J| \leq F \leq |I + J|$  and a quantisation axis projection  $m_F$  allow the eigenstates to be described using the  $|n, L, S, J, I, F, m_F\rangle$  basis. Since applied magnetic fields are not considered in this thesis the hyperfine states are  $m_F$  Zeeman degenerate, so only transitions between different  $F$  states are considered.

To visualise the gross, fine and hyperfine structures in caesium, the ground 6S and first excited state 6P splittings are shown in Fig. 2.7. The splittings are not drawn to scale and will be given in level schemes in the subsequent sections.

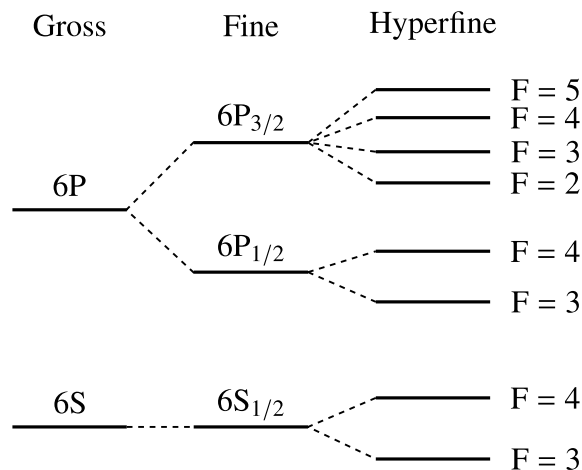


Figure 2.7: Gross, fine and hyperfine structure in the ground and first excited states of caesium. The fine and hyperfine splittings are not drawn to scale.

Finally, all  $F$  states in a hyperfine manifold decay with the same rate as dictated by fine structure [61]. The spontaneous decay rate for an individual transition from an upper state  $|n'\ell'\rangle$  to a lower state  $|n\ell\rangle$  is given by the Einstein  $A$  coefficient

$$A_{n'\ell',n\ell} = \frac{4\omega_{n'n}^3}{3\hbar c^3} \frac{\max(\ell', \ell)}{2\ell + 1} |\langle n'\ell' | er | n\ell \rangle|^2 . \quad (2.23)$$

The spontaneous decay rate  $\Gamma$  is then the sum of individual rates from dipole allowed upper state  $|n'\ell'\rangle$  to lower state  $|n\ell\rangle$  transitions as

$$\Gamma = \sum_{n\ell} A_{n'\ell',n\ell} . \quad (2.24)$$

## 2.4.2 Computing atomic properties

Modelling realistic systems requires hyperfine dipole moments  $\langle F'm_{F'} | e\mathbf{r} \cdot \hat{\mathbf{e}} | Fm_F \rangle$  to be calculated. This is greatly simplified via the Wigner-Eckart theorem, where matrix elements are factored into a product of a radial reduced matrix element and an angular Clebsch-Gordan coefficient [62]. The reduced element is further reduced through the  $F$ ,  $J$  and  $L$  bases leaving the calculation of a radial wavefunction overlap integral and a product of Wigner 3j and 6j symbols that arise when coupling angular momenta. This thesis uses a published Python package to perform such hierarchal calculations - the Alkali Rydberg Calculator (ARC) [63]. It fully documents the process of calculating matrix elements via application of the Wigner-Eckart theorem.

## 2.5 The Cs D1 line - theory and experiment

### 2.5.1 Theory

This section presents a model for the first accessible transition in caesium  $|6S_{1/2}\rangle \rightarrow |6P_{1/2}\rangle$  known as the D<sub>1</sub> line. The level scheme for the D<sub>1</sub> line in Fig. 2.8 is re-drawn from Ref. [64] with hyperfine splittings [65]. The spontaneous decay rate  $\Gamma$  and lifetime  $\tau$  of the  $6P_{1/2}$  state are  $\tau = 34.791(90)$  ns and  $\Gamma/(2\pi) = 4.575(12)$  MHz [37].

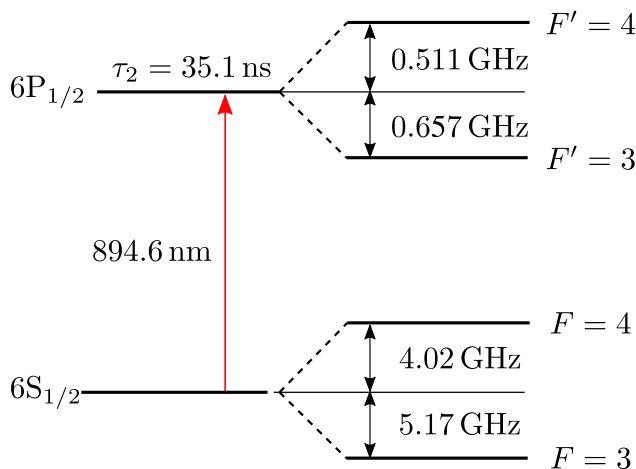


Figure 2.8: Representing the energy levels of the caesium D<sub>1</sub> line.

Transition frequencies are shifted to include level-dependent hyperfine shifts  $\omega_{\text{HFS}}$ , where an upper state  $F'$  and lower state  $F$  moves the resonance frequency as  $\omega_0 \rightarrow \omega_0 + \omega_{\text{HFS}}(F') - \omega_{\text{HFS}}(F)$ . Additionally, the selection rule  $F' - F = -1, 0, 1$  is obeyed for each transition leaving a maximum of three accessible upper  $F'$  states from an initial  $F$  state. In the weak probe regime, optical pumping is negligible such that individual transitions and absorption coefficients are considered separately. Here, the net absorption coefficient is modelled as a sum over individual transition absorptions through

$$\alpha = \frac{-2\omega_0 N}{c\epsilon_0 \hbar (2I+1)(2J+1)} \sum_{F=3}^4 \sum_{F'=3}^4 \sum_{m_F=-F}^F d_{Fm_F F'm_{F'}}^2 \int \text{Im} \left\{ \frac{\tilde{\rho}_{21}}{\Omega_1} \right\} f_g(v) dv . \quad (2.25)$$

The dividing prefactor  $(2I+1)(2J+1)$  averages over the degenerate Zeeman sub-level populations for each  $m_F$  transition. The dipole moment for the  $|Fm_F\rangle \rightarrow |F'm_{F'}\rangle$  is  $d_{Fm_F F'm_{F'}}$  and the first summation over  $F$  encodes the transition selection rule. By using the weak probe coherence (Eq. 2.13) with the Doppler shift  $\Delta \rightarrow \Delta - kv$ , the Voigt profile arises through the Doppler-averaging convolution integral of the Gaussian  $f_g(v)$  and the Lorentzian  $\text{Im}\{\tilde{\rho}_{21}\}$ .

The accuracy of Eq. 2.25 is tested against a published weak probe software package known as ElecSus [66, 67]. Figure 2.9 shows the superposition for a  $L = 75$  mm caesium vapour cell at  $T = 20^\circ\text{C}$ . The residuals show very good agreement to within 0.596% despite using equivalent expressions for the number density through same Antoine coefficients [35, 36]. However, the Python Fadeeva function [68] is used in ElecSus to calculate individual lineshapes, whereas the model here evaluates sums over velocity classes to approximate the Voigt integral. Secondly, ElecSus uses additional higher order terms in its hyperfine shift Hamiltonian to calculate shifts, whereas the literature values used here measure the hyperfine splittings directly using a mode locked laser [65].

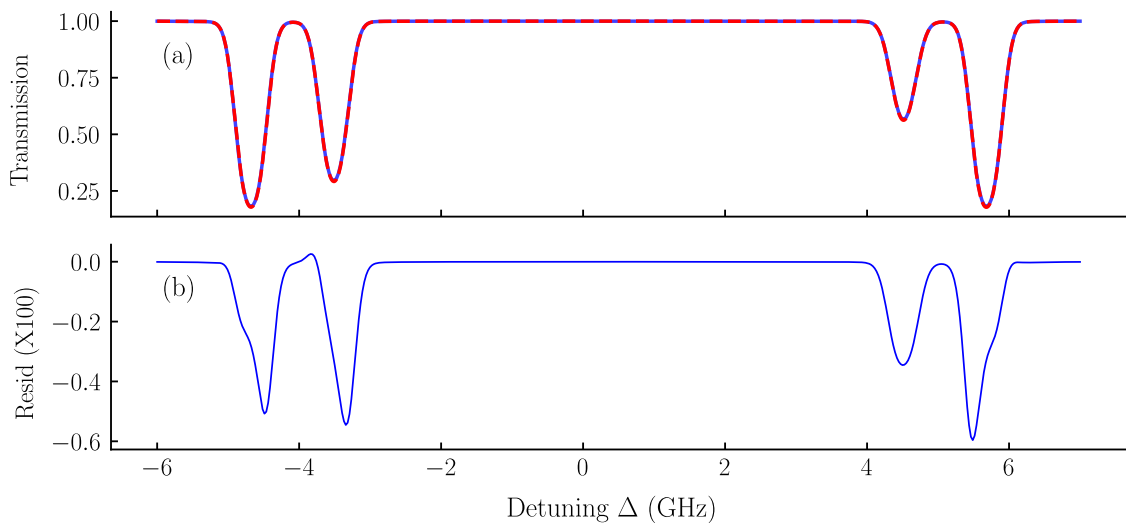


Figure 2.9: (a): ElecSus (red dashes) against the two-level model (solid blue) at  $T = 20^\circ\text{C}$  and  $L = 75$  mm, and (b): the residuals.

## 2.5.2 Experiment

The experimental setup for capturing the caesium  $D_1$  line transmission spectrum is given in Fig. 2.10. A Toptica DL Pro extended cavity diode laser (ECDL) is scanned across the 9.19 GHz-wide  $D_1$  line with a maximum output power of 125 mW. The power incident on the 75 mm bulk cell is reduced to  $P = 1\ \mu\text{W}$  through neutral density (ND) filtering and the  $\lambda/2$  waveplate and polarising beam splitter (PBS) pair allows for continuous transmitted power adjustment [69, 70].

From Eq. 2.14, for a beam with a FWHM of a few millimetres, the weak probe power is on the order of  $P_{\text{weak}} \approx 100\ \text{nW}$ . Each beam is focused onto a photodiode (PD) and data is captured on a digital storage oscilloscope. However, in this experiment the beam power is increased above the weak probe value to improve the PD signal signal-to-noise ratio (SNR). Voltage data was converted to transmission and the time data was calibrated against the nonlinearity of the laser scan using a low-finesse Fabry-Perot etalon - see Appendix A. The time data was then mapped to a frequency detuning axis and the transmission data was passed into ElecSus, which extracted an optimum temperature of  $T = 23.7^\circ\text{C}$  through fitting the normalised and linearised data.

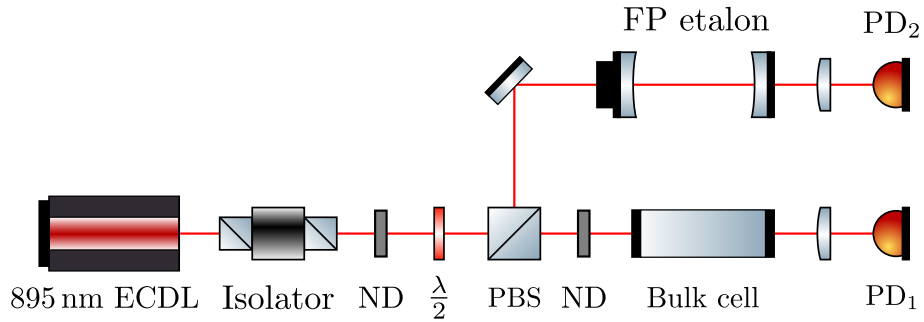


Figure 2.10: The experimental setup for acquiring the Cs  $D_1$  line transmission.

The data, theory and residuals are shown in Fig. 2.11, where residuals lie within 4%. The hyperfine  $F \rightarrow F'$  transitions are labelled above each respective transmission dip. Since atoms excited from one ground state can decay to the other far-detuned (9.19 GHz) ground state, they are effectively removed from the probe system. This hyperfine optical pumping is more efficient at reducing absorption than saturating a transition [71] and explains the increased transmission in the minima of the data as compared to the weak probe theory. To improve the  $D_1$  data, a low-noise high gain photodiode should be used with a weak probe beam to mitigate self- and hyperfine pumping.

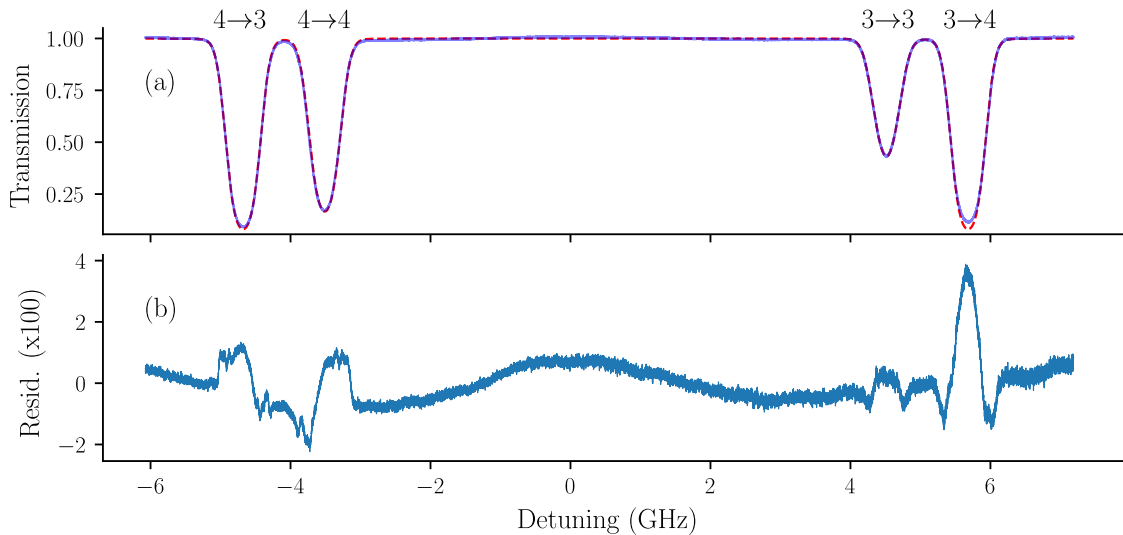


Figure 2.11: (a) the Cs  $D_1$  transmission spectrum (blue) at  $P = 1 \mu\text{W}$  versus ElecSus (red dashes). Differences (residuals) are multiplied by 100 and plotted in (b).

## 2.6 Exciting $6S_{1/2} \rightarrow 6P_{1/2} \rightarrow 6D_{3/2}$ in caesium

In this section, EIT in the caesium  $6S_{1/2} \rightarrow 6P_{1/2} \rightarrow 6D_{3/2}$  transition is investigated. A model is derived that recreates the EIT transmission features and forms the basis for the model describing the single-photon scheme presented in the next chapter.

### 2.6.1 Theory

The level scheme for the  $6S_{1/2} \rightarrow 6P_{1/2} \rightarrow 6D_{3/2}$  transition is given in Fig. 2.12, which shows the transition wavelengths, lifetimes and hyperfine splittings [37, 72–74] with the 894.6 nm probe and 876.4 nm coupling beams. The decay pathway  $6D_{3/2} \rightarrow 7P_{1/2}$  at 12.14  $\mu\text{m}$  then leads to  $7P_{1/2} \rightarrow 6S_{1/2}$  at 459.4 nm. This visibly blue fluorescence will be compared to the probe EIT spectrum to show how fluorescence is maximised in EIT despite an increased resonant probe transparency.

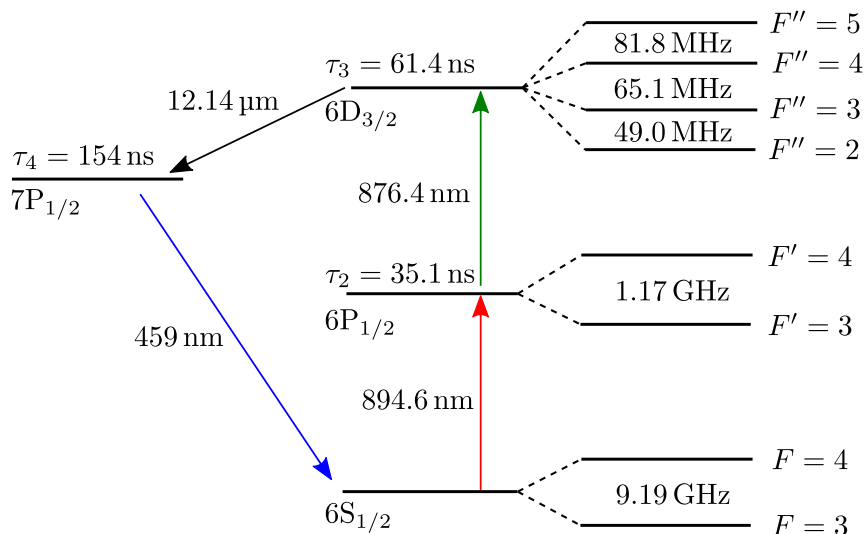


Figure 2.12: The caesium energy level diagram studied in this section with transition wavelengths, natural lifetimes, fine and hyperfine structure.

EIT is a two-step, dipole-allowed, one-photon coherence effect that leads to an increased probe transparency at two-photon resonance [55]. However, three-level ladder systems can also host two-photon absorption (TPA) [75], which is a two-photon coherence effect where the parity forbidden  $F, m_F \rightarrow F'', m_{F''}$  transition occurs. Due to the large caesium ground-state splitting of 9.19 GHz, transitions

from  $F = 3$  and  $F = 4$  are considered separately. These are illustrated in Fig. 2.13, which shows the accessible transitions from the  $\Delta F = -1, 0, 1$  selection rule. Labels (i) to (iii) represent three hyperfine EIT transitions for  $F'' = 2, 3, 4$  and (iv) to (vi) represent  $F'' = 3, 4, 5$ .

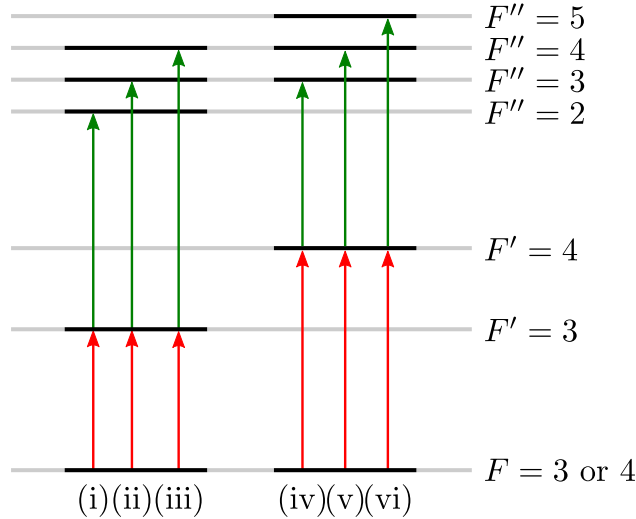


Figure 2.13: Visualising the dipole-allowed transitions in  $6S_{1/2} \rightarrow 6P_{1/2} \rightarrow 6D_{3/2}$  given the selection rule  $\Delta F = -1, 0, 1$ .

Accounting for hyperfine and Doppler shifts, the two-photon resonance condition for probe and coupling detunings  $\Delta_{1,2}$  and wavevectors  $\mathbf{k}_{1,2}$  is

$$\Delta_1 + \Delta_2 - (\mathbf{k}_1 + \mathbf{k}_2) \cdot \mathbf{v} + \omega_{\text{HFS}}(F) - \omega_{\text{HFS}}(F'') = 0. \quad (2.26)$$

This equation is independent of the middle state hyperfine shift  $\omega_{\text{HFS}}(F')$  because the probe and coupling detunings are shifted by  $\mp\omega_{\text{HFS}}(F')$  respectively, so the terms cancel when added together. In TPA, one-photon resonances need not occur, so multiple velocities exist that satisfy Eq. 2.26. From Fig. 2.13 it is therefore expected that three EIT peaks occur at one- and two-photon resonances and four TPA peaks occur in general two-photon resonance conditions.

To include the effects of hyperfine structure in modelling the absorption coefficient, the three-level coherence  $\tilde{\rho}_{21}$  is augmented to account for the three accessible  $F''$  states from a given  $F'$  state. By constructing a five-level Hamiltonian repre-

senting a single ground, a single middle and the three accessible excited states [76] and applying the weak probe limit allows the inclusion of a net effective angular frequency [77]. Denoting it here as  $\omega_{\text{eff}}$  gives the three-level hyperfine coherence as

$$\tilde{\rho}_{21} = \frac{-i\Omega_{Fm_F F'm_{F'}}}{\Gamma_2 - 2i(\Delta_1 - \mathbf{k}_1 \cdot \mathbf{v} + \omega_{\text{HFS}}(F) - \omega_{\text{HFS}}(F')) + \omega_{\text{eff}}}, \quad (2.27)$$

with the inclusion of hyperfine structure in the following term

$$\omega_{\text{eff}} = \sum_{F''=F'-1}^{F'+1} \frac{\Omega_{F'm_{F'} F''m_{F''}}^2}{\Gamma_3 - 2i(\Delta_1 + \Delta_2 - (\mathbf{k}_1 + \mathbf{k}_2) \cdot \mathbf{v} + \omega_{\text{HFS}}(F) - \omega_{\text{HFS}}(F''))}. \quad (2.28)$$

The Rabi frequencies for the two transitions are  $\Omega_{Fm_F F'm_{F'}}$  and  $\Omega_{F'm_{F'} F''m_{F''}}$ , respectively. By then using this three-level coherence in the expression for the absorption coefficient in Eq. 2.25, a weak probe Doppler-averaged hyperfine EIT model is made. Beams are assumed to induce  $\Delta m_F = 0$  transitions.

The analysis above assumed constant Rabi frequencies from uniform intensity beams, but the lasers used in this thesis have a Gaussian intensity profile. This implies an over-estimate of the Rabi frequency that atoms experience. Consequently, the hyperfine EIT and two-photon absorption peaks will be larger in theory than in experiment. Additionally, the interaction time of atoms with the probe beam is approximated by calculating the reciprocal of the mean transit time through a Gaussian beam of a  $1/e^2$  waist  $w_0$ . When an atom leaves the probe beam it is assumed to leave the excitation region, so every level is coupled to the ground state with a transit time decay  $\Gamma_{\text{tt}}$  [78] of

$$\Gamma_{\text{tt}} = \frac{2}{\omega_0} \sqrt{\frac{k_B T}{\pi m \ln(2)}}. \quad (2.29)$$

Mathematically,  $\Gamma_{\text{tt}}$  is added to the existing spontaneous decays, which reduces EIT peak visibilities. For room-temperature thermal vapours and beams with millimetre-scale  $1/e^2$  waists the transit time decay scales as  $\Gamma_{\text{tt}}/(2\pi) \sim 10$  kHz whereas the

spontaneous decays  $\Gamma_{2,3}/(2\pi)$  in  $6P_{1/2}$  and  $6D_{3/2}$  scale as megahertz. When beams are focused to tens of microns or below the transit time broadening scales similarly to the spontaneous decay rates.

## 2.6.2 Experiment

Shown in Fig. 2.14 is the optical layout, where a weak 895 nm probe and a strong 876 nm coupling beam counter-propagate through a 75 mm room-temperature caesium vapour cell. The probe was scanned about  $6S_{1/2} \rightarrow 6P_{1/2}$  and the coupling laser was detuned about the different  $6P_{1/2} \rightarrow 6D_{3/2}$  hyperfine resonances and free-run.

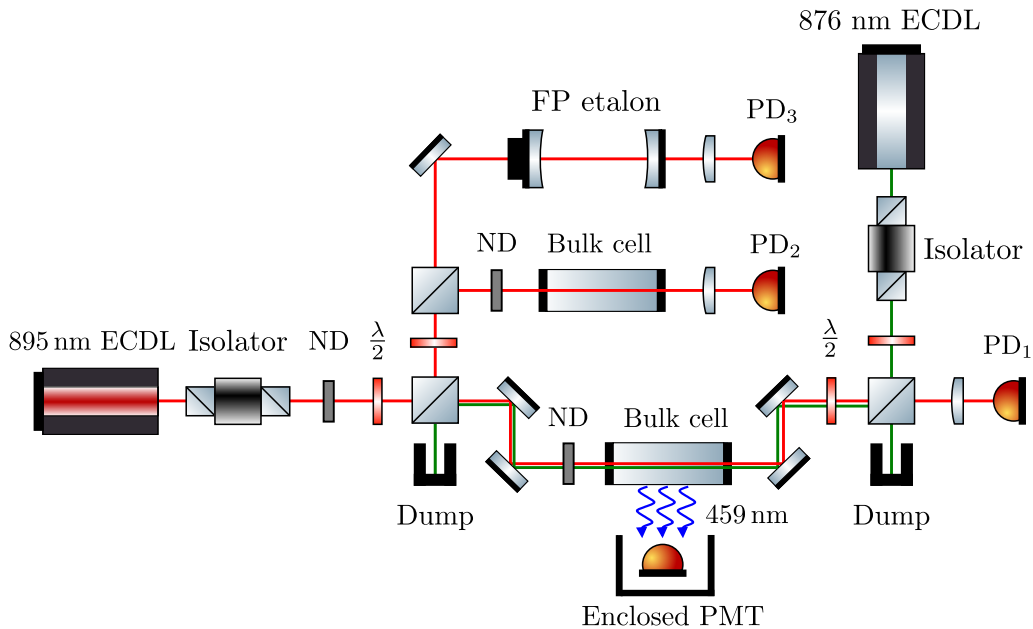


Figure 2.14: The optical layout for capturing probe EIT transmission and 459 nm fluorescence data from a 75 mm caesium bulk cell.

The Toptica DL Pro probe beam was passed through an optical fibre to recover a Gaussian mode with  $(w_{1/e^2})_x = (w_{1/e^2})_y = 1$  mm. A second bulk cell was used with the low-finesse Fabry-Perot etalon for time axis calibration and time/frequency mapping - see Appendix A. The coupling beam was derived from a Moglabs cat-eye ECDL with  $(w_{1/e^2})_x = 1$  and  $(w_{1/e^2})_y = 1.5$  mm with a stable output mode power of  $P_c \approx 30$  mW after the optical isolator. The two beams counter-propagated in the main cell, the probe was detected on photodiode 1 (PD<sub>1</sub>) and the 459 nm fluorescence

was band-pass filtered and captured on an enclosed photomultiplier tube (PMT).

Figure. 2.15 shows EIT features centred in the left-hand  $D_1$  dip ( $F = 4 \rightarrow 3$ ). Transmission data from (a) was taken at  $P_p = 15 \mu\text{W}$  and is zoomed to give (b) with a superposition from the EIT model in Eq. 2.27, and the corresponding fluorescence data in (c) with  $P_p = 300 \mu\text{W}$  was superimposed with a multi-peak Voigt function. Due to the large ground state  $6S_{1/2}$   $F = 3, 4$  hyperfine splitting of 9.19 GHz there are two sets of two Doppler-broadened dips from  $6P_{1/2}$  and two sets of hyperfine features from the  $6D_{3/2}$   $F'' = 2, 3, 4, 5$  splitting. Therefore the  $F = 3$  and 4 dips are considered separately.

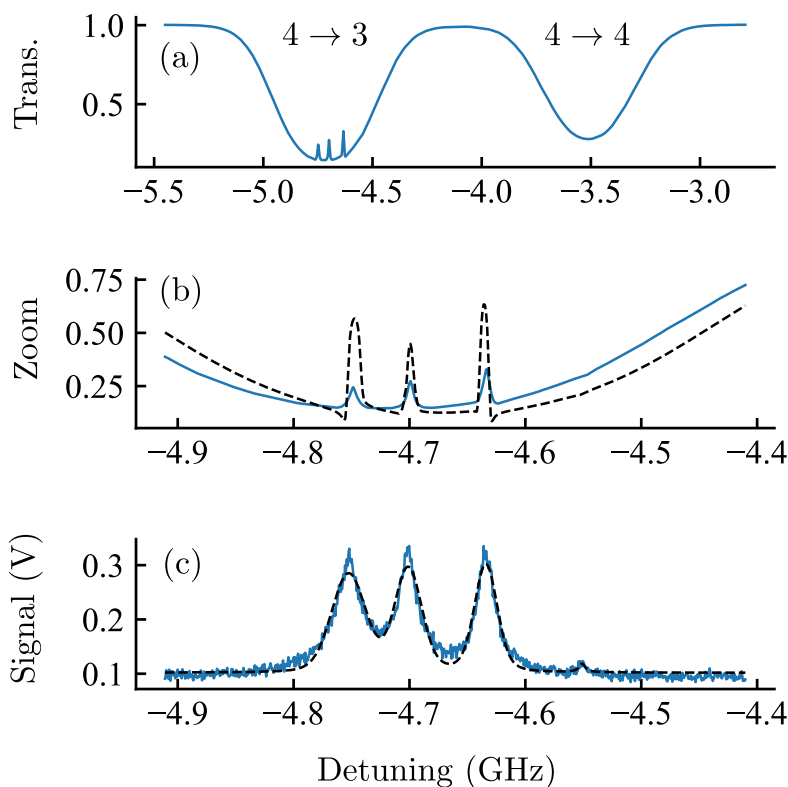


Figure 2.15: (a): data for the  $F'' = 2, 3, 4$  EIT peaks with  $P_p = 15 \mu\text{W}$  and  $P_c = 30 \text{mW}$ . The EIT model in black dashes with  $T = 15^\circ\text{C}$  and  $P_c = 30 \text{mW}$  (b) and fluorescence data at  $P_p = 300 \mu\text{W}$  with its Voigt fit in (c).

Three EIT peaks ( $F'' = 2, 3, 4$ ) and a small right-hand TPA peak ( $F'' = 5$ ) are seen in Fig. 2.15(a) because the coupling laser detuning knob made it challenging to create perfectly resonant EIT. The model (black dashes) in (b) over-estimates peak heights and widths, and predicts sharp wing-like dips on the edges of each

transmission peak that are very weakly seen in the data. Figure 2.16 shows an example transition from EIT to TPA for off-resonance peaks, where four peaks are visible. The three main peak heights and widths are over-estimated and Voigt profiles are fitted to the fluorescence peaks in (c), where the signal magnitude is lower than the EIT fluorescence peak signal in Fig. 2.15. Since fluorescence is proportional to the excited state population, away from resonant EIT the number of excited state atoms is lower thereby reducing the fluorescence.

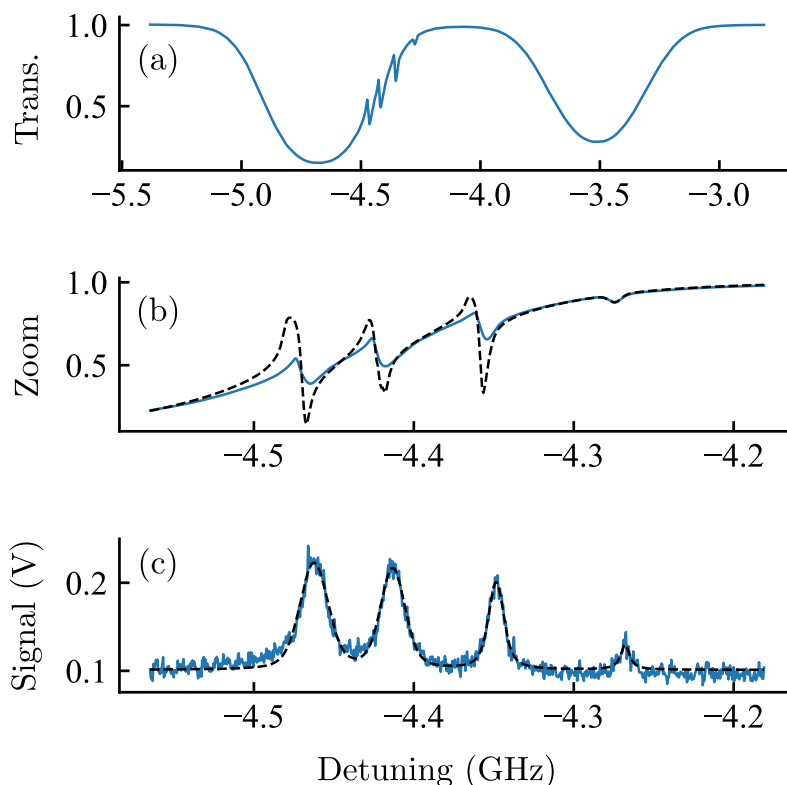


Figure 2.16: (a): TPA  $F'' = 2, 3, 4, 5$  peaks with  $P_p = 15 \mu\text{W}$  and  $P_c = 30 \text{ mW}$ . The model at  $\Delta_c/(2\pi) = 0.339 \text{ GHz}$  in black dashes (b) and fluorescence data at  $P_p = 300 \mu\text{W}$  with its Voigt fit in (c).

Theory and experiment likely differ because the Moglabs ECDL operated at a diode current that yielded a lower power mode. Secondly, the non-weak probe, which gave power-broadened features, so in future a higher gain photodiode should be used with  $P_p < 1 \mu\text{W}$ . Thirdly, the optical Bloch equations should be solved to account for optical pumping [41, 79] and a loss state should be included to model decays to the ground state outside of the level scheme. Finally, simulations should be

averaged across position in a Gaussian beam intensity profile, which would remove the uniform beam assumption and potentially recover realistic peak heights.

Waterfall plots in in Fig. 2.17 show fluorescence versus  $\Delta_p$  and  $\Delta_c$  at  $P_p = 300 \mu\text{W}$  and  $P_c = 30 \text{mW}$  for (a)  $F = 4 \rightarrow F' = 3, 4$  and (b)  $F = 3 \rightarrow F' = 3, 4$ . For EIT at positions three and seven, a smaller unwanted fourth peak is visible due to imperfect  $\Delta_c$  adjustment. Further from resonance the TPA peaks expectedly weaken because fewer atoms exist that have velocities to undergo Doppler-shifts onto TP resonance. Fluorescence is largest in EIT when the  $6D_{3/2}$  population and the decay through  $6D_{3/2} \rightarrow 7P_{1/2} \rightarrow 6S_{1/2}$  are maximised. Outside of TP resonance, absorption increases but the  $6D_{3/2}$  population and the fluorescence reduce.

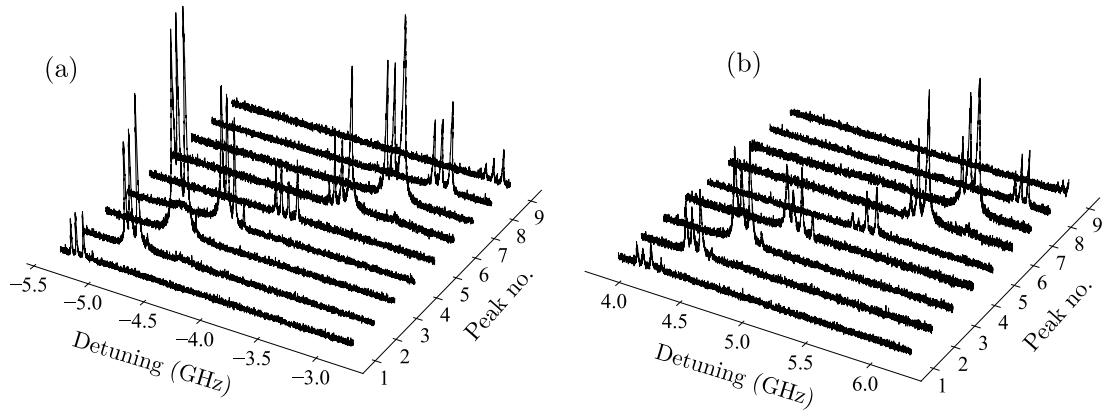


Figure 2.17: Evolution of 459.4 nm fluorescence for different coupling detunings with  $P_p = 300 \mu\text{W}$  and  $P_c = 30 \text{mW}$  for (a):  $F = 4 \rightarrow F' = 3, 4$  and (b):  $F = 3 \rightarrow F' = 3, 4$ . Positions three and seven represent EIT and everywhere else is TPA.

Figure 2.17 is then used to extract the  $6D_{3/2}$  hyperfine splitting separations. Using the larger fluorescence peaks of Fig. 2.17(a), Voigt profiles were fitted to all nine traces to give Fig. 2.18. Certain peak SNRs were too low for the Voigt fitting to recognise them, so only seven data points were available for the  $F'' = 2, 3$  and  $F'' = 4, 5$  splittings whilst nine were available for  $F'' = 3, 4$ . The means and standard errors  $\alpha = \sigma_{N-1}/\sqrt{N}$  [80] of the splittings were calculated and displayed in Table 2.1 in agreement with measurements from Ref. [72] to within one error bar. Including peak data from (b) would further reduce the error bar sizes.

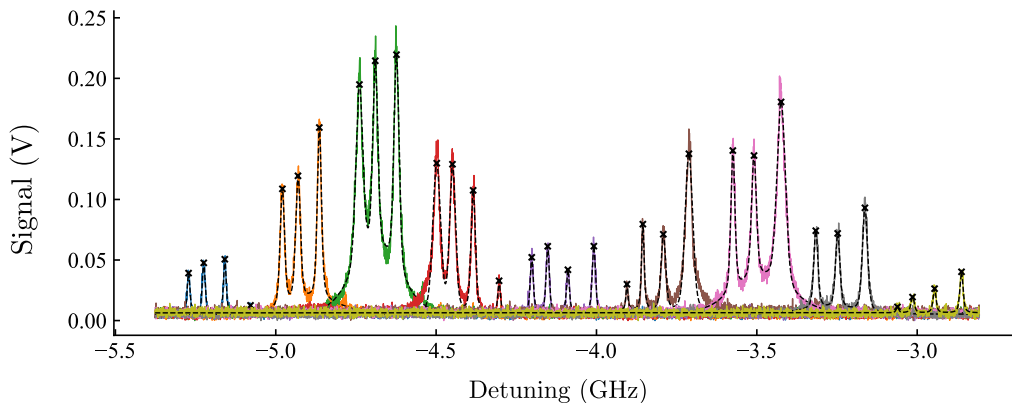


Figure 2.18: A side view of the left-hand fluorescence waterfall plot in Fig. 2.17(a) across the nine  $F = 4 \rightarrow F' = 3, 4$  locations. Voigt profiles (black dashes) are fitted to each trace and their peaks are marked in crosses.

$F''$ Interval	This thesis	Ref. [72]
$4 \rightarrow 5$	$82.2 \pm 0.8$	$81.8 \pm 0.1$
$3 \rightarrow 4$	$65.6 \pm 0.6$	$65.1 \pm 0.2$
$2 \rightarrow 3$	$48.6 \pm 0.4$	$49.0 \pm 0.1$

Table 2.1: Comparing measured  $6D_{3/2}$  hyperfine splittings in MHz with Ref. [72].

## 2.7 Summary

This chapter analysed EIT and fluorescence data from a room-temperature 75 mm caesium bulk cell for the  $6S_{1/2} \rightarrow 6P_{1/2} \rightarrow 6D_{3/2}$  transition and  $7P_{1/2} \rightarrow 6S_{1/2}$  decay. The EIT data was compared to a derived model, which correctly captured the transition from EIT to two-photon absorption and gave visual peak height and width agreement. The  $6D_{3/2}$  hyperfine splittings were extracted from fluorescence measurements and agreed with previous literature to within one error bar. EIT resulted in an increased resonant probe transmission as well as a maximised upper state population, as seen in the fluorescence spectra. This result is fundamental to the next chapter where EIT is motivated as a platform for exciting atoms to Rydberg levels in a three-beam single-photon emitter and storage scheme.

# Chapter 3

## Zero-wave vector Rydberg polaritons

This chapter details the single photon storage mechanism considered in this thesis based on a Doppler-free three-photon Rydberg ladder excitation scheme. Laser parameters are calculated and a custom thermal vapour cuvette is presented for minimised focal astigmatism Doppler-free excitation. Finally, components of the potential future experimental layout are proposed.

### 3.1 Introduction: single-photon storage scheme

The proposed single photon emitter scheme also inherently includes a photon storage mechanism. It relies on storing a weak incident probe pulse before emitting a single photon of the same wavelength, spatial mode and direction as the incident pulse. To understand the proposed scheme, three key background topics are first covered: dark-state polaritons, the Rydberg blockade and uniform-phase spin waves. Thereafter the relevant laser excitation scheme is presented and reference is made back to these three key background topics.

### 3.1.1 Dark-state polaritons

In the proposed single-photon emitter scheme, a photon is first stored as a dark-state polariton [11] via ladder EIT [51–55] in a thermal vapour before being deterministically emitted. Consider a quantum field representing a probe pulse propagating along the  $z$ -axis with temporal dependence  $\hat{\mathcal{E}}(z, t)$  and a classical control field  $\Omega(t)$  that together satisfy the conditions for EIT described in Section 2.2.2. The pulse couples the ground and first excited states  $|1\rangle$  and  $|2\rangle$  and the classical field couples  $|2\rangle$  to the upper state  $|3\rangle$ , as shown in Fig. 3.1.

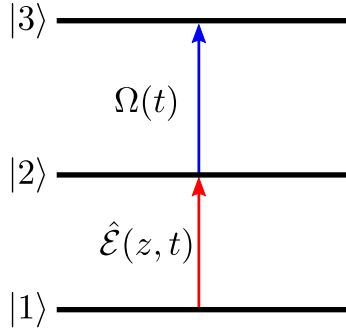


Figure 3.1: The EIT ladder scheme used to store a weak probe pulse (red) as a polariton by adiabatically reducing the control field (blue) to zero.

If the probe field’s Rabi frequency is much smaller than the control field Rabi frequency  $\Omega(t)$ , and  $\Omega(t)$  changes adiabatically then a first-order perturbation expansion yields a propagation equation for the probe pulse [11] as

$$\left(\frac{\partial}{\partial t} + c\frac{\partial}{\partial z}\right)\hat{\mathcal{E}}(z, t) = -\frac{g^2 N}{\Omega(t)}\frac{\partial}{\partial t}\left(\frac{\hat{\mathcal{E}}(z, t)}{\Omega(t)}\right), \quad (3.1)$$

with the number of atoms  $N$  in an excitation volume  $V$ , an atom-light coupling constant  $g^2 = \omega_0 d_{21}^2 / (2\hbar\epsilon_0 V)$  and the  $|1\rangle \rightarrow |2\rangle$  resonance frequency  $\omega_0$ . Under these conditions, a canonical transformation can be made by introducing a new quantum field  $\hat{\Psi}(z, t)$  that encodes both the optical field  $\hat{\mathcal{E}}$  and the atomic excitations using the operator  $\hat{\sigma}_{23}(z, t)$  constructed from raising and lowering operators via

$$\hat{\Psi}(z, t) = \hat{\mathcal{E}}(z, t) \cos \theta(t) - \hat{\sigma}_{23}(z, t) \sqrt{N} \sin \theta(t). \quad (3.2)$$

The mixing angles follow  $\tan\theta(t) = g\sqrt{N}/\Omega(t)$  and  $\hat{\Psi}(z, t)$  satisfies a transformed equation of motion describing a new field with shape-preserving propagation at a group velocity  $v_g/c = \cos^2\theta(t)$ . From Eq. 3.2, adiabatically turning off the control field  $\Omega$  causes  $\theta$  to follow  $0 \rightarrow \pi/2$  and the group velocity  $v_g$  decreases to zero. Consequently, the field  $\hat{\Psi}(z, t)$  changes from an optical excitation to a purely matter excitation representing the deceleration of the input pulse and storage of its pulse shape and quantum state as a collective excitation.

This quantum field also has bosonic commutation relations [11], so it is associated with a bosonic quasiparticle denoted as a polariton. Furthermore, the number states created by  $\hat{\Psi}(z, t)$  do not contain the upper state  $|3\rangle$  and are eigenstates of the atom-light interaction Hamiltonian with eigenenergies of zero. These states are theoretically immune to spontaneous emission and are therefore dark states allowing these quasi-particles to be known as dark-state polaritons.

### 3.1.2 The Rydberg blockade

The properties of Rydberg atoms can be exploited to ensure that only a single photon is stored as the collective excitation dark-state polariton. Atoms that have a valence electron with principal quantum numbers  $n > 10$  are Rydberg atoms [81] and have tunable properties that scale with  $n$ , as seen in Table 3.1 [82]. Most notably the Rydberg-Rydberg dipole moment scales with  $n^2$ , which forms the basis of the Rydberg blockade where all but singly excited collective states are suppressed [31].

Property	Scaling
Binding energy	$n^{-2}$
Radius	$n^2$
Dipole moment: Rydberg to Rydberg	$n^2$
Dipole moment: Rydberg to ground	$n^{-3/2}$
Radiative lifetime	$n^3$

Table 3.1: Rydberg atom scaling properties with the principal quantum number,  $n$ .

To explain the blockade consider a two-atom collective ground state  $|gg\rangle$ . A single Rydberg excitation has the pair states  $|gr\rangle$  and  $|rg\rangle$ , coupled to  $|gg\rangle$  with a resonant Rabi frequency  $\Omega$ . However, when two atoms are excited to the same Rydberg state  $|rr\rangle$  they experience dipole-dipole interactions when the separation distance  $R$  exceeds the extent of the Rydberg electronic wavefunction [83]. The resulting pair state energy is shifted by a second-order perturbative van der Waals term  $\Delta E_{\text{dd}} = \hbar C_6/R^6$  where  $C_6$  scales very favourably as  $n^{11}$ . For sufficiently large  $n$  or small  $R$  the shift exceeds the Rabi frequency of the excitation laser  $\Omega$  as  $\hbar C_6/R^6 > \hbar\Omega$  giving a blockade  $R_b$  of

$$R_b = \left( \frac{C_6}{\Omega} \right)^{1/6}. \quad (3.3)$$

Therefore, for atoms within the blockade sphere it is expected that only a singly excited collective state can occur. The shift-induced blockade is visualised in Fig. 3.2 and the argument extends to more than two atoms.

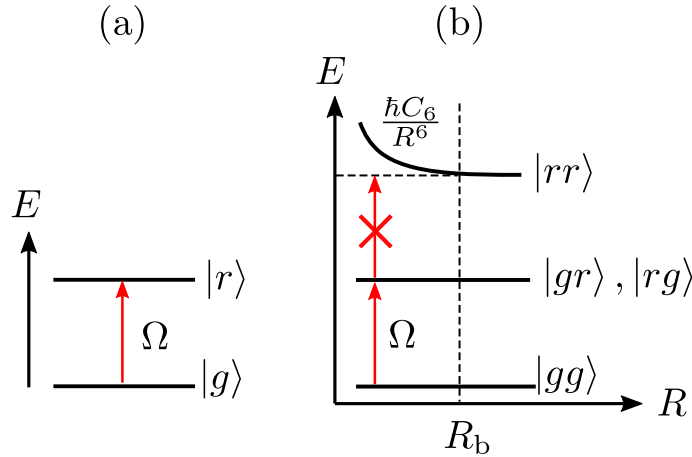


Figure 3.2: A single atom excited to a Rydberg state  $|r\rangle$  (a) and the position-dependent vdW shift preventing doubly excited Rydberg states (b). The laser Rabi frequency is  $\Omega$  and the blockade radius is  $R_b$ .

### 3.1.3 Uniform phase spin waves

Dark-state polaritons have now been described as a mixture of an electromagnetic wave and collective atomic excitations. This is known as a spin wave [84] and for a singly excited collective state the symmetric wavefunction is

$$|\psi\rangle = \frac{1}{\sqrt{N}} \sum_{j=1}^N e^{i\mathbf{k}\cdot\mathbf{r}_j} |g_1 \dots r_j \dots g_N\rangle , \quad (3.4)$$

with  $N$  atoms of position vectors  $\mathbf{r}_j$  and  $\mathbf{k}$  is the sum of incident wave vectors when exciting to the Rydberg level  $|r\rangle$ . The summation is the coherent superposition of the  $j^{\text{th}}$  atom being in the Rydberg state  $|r_j\rangle$  with others being in the ground state.

The Rydberg polaritonic wavefunction in Eq. 3.4 shows that the input optical field is stored amongst the phases of the atomic distribution within the blockade radius at zero time ( $t = 0$ ). However the atomic positions  $\mathbf{r}_j$  and relative phases change with time in thermal vapours, which changes the spatial mode and worsens the directionality and efficiency of the photon readout [85]. This motional dephasing limits the polariton storage lifetime with timescales  $\tau_{\text{deph}}$  on the order of

$$\tau_{\text{deph}} = \frac{2\pi}{u\|\mathbf{k}\|} , \quad (3.5)$$

with the most probable atomic speed  $u = \sqrt{2k_B T/m}$ .

To counter motional dephasing, the total wavevector can be set to  $\mathbf{k} = \mathbf{0}$  by applying three or more excitation fields where each atom obtains the same relative phase irrespective of its time-dependent position  $\mathbf{r}_j$ . This creates a uniform phase spin wave [13] because  $\mathbf{k}\cdot\mathbf{r}_j$  will be zero for all atomic positions. This zero wave vector polariton is created by using three beams in a four-level ladder scheme presented in the next section. The experimental reality of overlapping three focused beams in a vapour cell whilst simultaneously achieving a zero wave vector is also discussed.

## 3.2 Doppler-free Rydberg excitation

A three-beam zero wave vector requires a four-level ladder scheme, which is presented in this section. Incidence angles for the three beams are calculated, conditions for EIT are derived to map the probe pulse to a Rydberg polariton and the probe Doppler-averaged transmission is simulated.

### 3.2.1 Excitation laser angles

The fine structure caesium level scheme for a three-beam zero wave vector is shown in Fig. 3.3. The transitions are visualised in (a) as  $6S_{1/2} \rightarrow 6P_{1/2}$  via a  $\lambda_p = 894.6$  nm probe beam to  $6P_{1/2} \rightarrow 7S_{1/2}$  via a  $\lambda_d = 1359$  nm dressing beam to  $7S_{1/2} \rightarrow nP$  with a variable coupling beam wavelength  $\lambda_c$  as a function of the target Rydberg principal quantum number  $n$ . Fig. 3.3(b) shows that the dressing and coupling beam angles are defined relative to the probe beam such that  $\mathbf{k}_p + \mathbf{k}_d + \mathbf{k}_c = \mathbf{0}$  for the zero wave vector. The probe ( $\mathbf{k}_p$ ), dressing ( $\mathbf{k}_d$ ) and coupling wave vectors ( $\mathbf{k}_c$ ) are assumed to be two-component vectors in-plane with the optical table.

By considering the horizontal and vertical components of the zero wave vector condition with a fixed probe and dressing wavelength the relative angles  $\theta_d$  and  $\theta_c$  can be found in terms of the variable  $\lambda_c$  as

$$\cos \theta_d = \frac{\lambda_p \lambda_d}{2} \left( \frac{1}{\lambda_p^2} + \frac{1}{\lambda_d^2} - \frac{1}{\lambda_c^2} \right), \quad (3.6a)$$

$$\cos \theta_c = \frac{\lambda_p \lambda_c}{2} \left( \frac{1}{\lambda_p^2} + \frac{1}{\lambda_c^2} - \frac{1}{\lambda_d^2} \right). \quad (3.6b)$$

For alkali metals, the semi-empirical hydrogenic Rydberg-Ritz formula [86] describes the binding energies of a fine structure state  $|nLJ\rangle$  as

$$E(n, L, J) = -\frac{R_\infty}{(n - \delta(n, L, J))^2}, \quad (3.7)$$

with  $R_\infty \approx 13.6$  eV and a state-dependent correction term known as the quantum

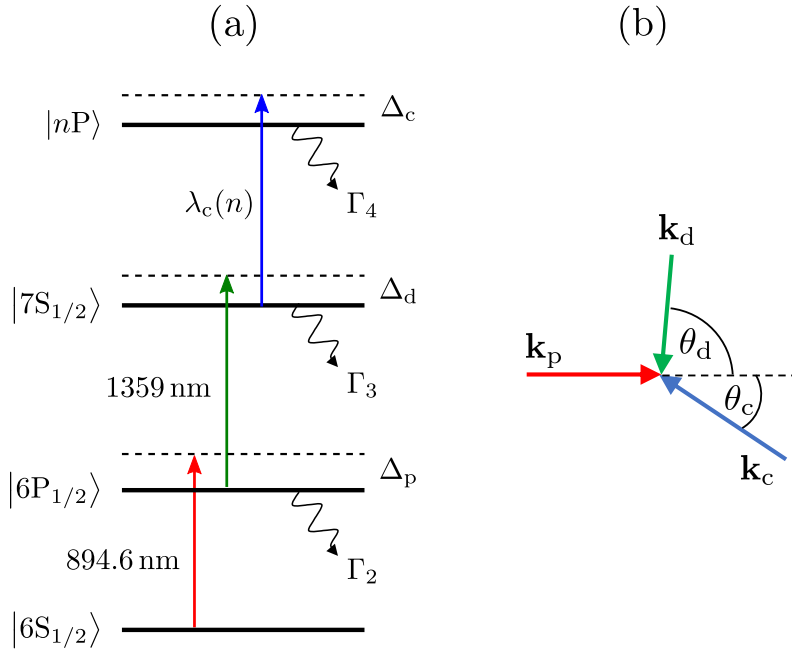


Figure 3.3: (a): Representing the four-level ladder scheme to excite to the variable Rydberg state  $|nP\rangle$  using probe (red), dressing (green) and coupling (blue) beams. Right (b): visualising the probe, dressing and coupling beams with a common overlap and angles relative to the probe wave vector.

defect  $\delta(n, L, J)$ . The defect decreases as  $L$  increases because the electron has a higher probability of being found at larger radii thereby reducing the interaction strength with the inner core electrons. Defects are experimentally found by fitting to the expansion  $\delta(n, L, J) = \sum_{n=0} \delta_{2n}/(n - \delta_0)^{2n}$  and for the heavier alkali metals,  $\delta \approx 0$  for  $L \geq 3$  [87]. This gives a coupling wavelength from a lower state  $|n'L'J'\rangle$  to the target Rydberg state  $|nLJ\rangle$  of

$$\lambda_c(n) = \frac{hc}{E(n, L, J) - E(n', L', J')}, \quad (3.8)$$

where  $h$  and  $c$  are Planck's constant and the speed of light in a vacuum. This expression for  $\lambda_c(n)$  is then used in Eq. 3.6 to give the required  $\theta_{d, c}$  for a target  $n$ .

The Rydberg transition wavelength  $\lambda_c$  for a target principal quantum number  $n$  and the resulting  $\theta_{d, c}$  are plotted in Fig. 3.4 for an example Rydberg state  $|nP_{1/2}\rangle$  from  $|7S_{1/2}\rangle$ . Transition wavelengths were calculated using Ref. [63] and the limiting wavelengths and angles are  $\lambda_c = 776.94$  nm,  $\theta_d = 85.32^\circ$  and  $\theta_c = 34.73^\circ$ . This allows

the required Rydberg wavelength and beam incidence angles to be calculated for a target Rydberg state.

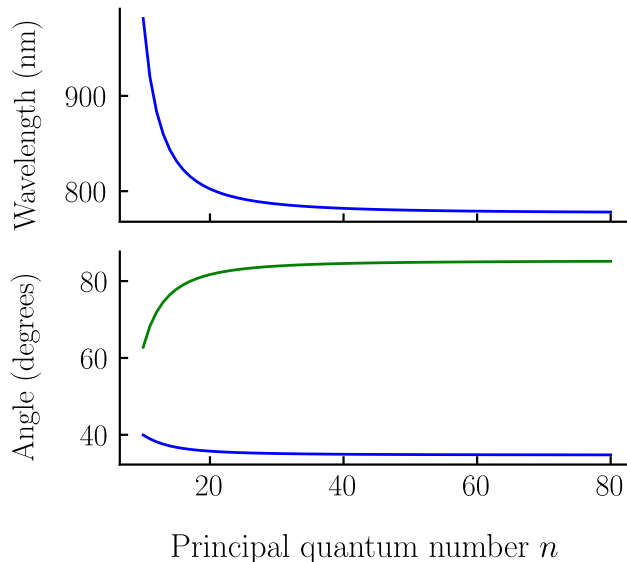


Figure 3.4: Upper panel: Rydberg transition wavelengths (blue) to state  $|nP_{1/2}\rangle$  from  $|7S_{1/2}\rangle$ . Lower panel: dressing (green) and coupling (blue) angles for zero-wave excitation given the target Rydberg state  $n$ .

Since the beams overlap at nonzero angles they create a finite interaction volume, whose equivalent spherical radius should ideally resemble the blockade radius. Parameters for this condition are calculated in Section 3.3.2. The weak probe pulse is stored as a Rydberg polariton via EIT where it propagates through the thermal vapour before it reaches the excitation region. The already weak probe is absorbed by the gas during propagation and is heavily attenuated, so a potential solution is off-resonant dressed state EIT, which is derived in the next subsection.

### 3.2.2 Dressed-state EIT

Conditions for four-level EIT are derived here using the basis states  $|1\rangle$ ,  $|2\rangle$ ,  $|3\rangle$  and  $|4\rangle$ . The probe, dressing and coupling detunings and Rabi frequencies are  $\Delta_p$ ,  $\Delta_d$ ,  $\Delta_c$

and  $\Omega_p, \Omega_d, \Omega_c$ , and in the rotating wave approximation, the system Hamiltonian is

$$\tilde{H} = \frac{\hbar}{2} \begin{pmatrix} 0 & \Omega_p & 0 & 0 \\ \Omega_p & -2\Delta_p & \Omega_d & 0 \\ 0 & \Omega_d & -2(\Delta_p + \Delta_d) & \Omega_c \\ 0 & 0 & \Omega_c & -2(\Delta_p + \Delta_d + \Delta_c) \end{pmatrix}, \quad (3.9)$$

and with natural decay rates  $\Gamma_i$  for state  $|i\rangle$  the phenomenological decay matrix is

$$\mathcal{L} = \frac{1}{2} \begin{pmatrix} 2\Gamma_2\rho_{22} & -\Gamma_2\tilde{\rho}_{12} & -\Gamma_3\tilde{\rho}_{13} & -\Gamma_4\tilde{\rho}_{14} \\ -\Gamma_2\tilde{\rho}_{21} & 2(\Gamma_3\rho_{33} - \Gamma_2\rho_{22}) & -(\Gamma_2 + \Gamma_3)\tilde{\rho}_{23} & -(\Gamma_2 + \Gamma_4)\tilde{\rho}_{24} \\ -\Gamma_3\tilde{\rho}_{31} & -(\Gamma_2 + \Gamma_3)\tilde{\rho}_{32} & 2(\Gamma_4\rho_{44} - \Gamma_3\rho_{33}) & -(\Gamma_3 + \Gamma_4)\tilde{\rho}_{34} \\ -\Gamma_4\tilde{\rho}_{41} & -(\Gamma_2 + \Gamma_4)\tilde{\rho}_{42} & -(\Gamma_3 + \Gamma_4)\tilde{\rho}_{43} & -2\Gamma_4\rho_{44} \end{pmatrix}. \quad (3.10)$$

By extending the methodology to find the three-level weak probe coherence  $\tilde{\rho}_{21}$  from Ref. [55], the four-level coherence is found to be

$$\tilde{\rho}_{21} = \frac{-i\Omega_p}{\Gamma_2 - 2i\Delta_p + \frac{\Omega_d^2}{\Gamma_3 - 2i(\Delta_p + \Delta_d) + \frac{\Omega_c^2}{\Gamma_4 - 2i(\Delta_p + \Delta_d + \Delta_c)}}}. \quad (3.11)$$

For three levels, EIT occurs for two-photon resonance and increases in strength with the second beam Rabi frequency. Correspondingly, the effects of a zero dressing and coupling detuning is investigated by plotting the normalised imaginary component of the weak probe susceptibility  $\chi_I/\chi_0$  against the normalised probe detuning  $\Delta_p/\Gamma_2$  in Fig. 3.5. The normalised decay rates are fixed at  $\Gamma_3/\Gamma_2 = 0.01$  and  $\Gamma_4/\Gamma_2 = 0.001$ . Panels (a) to (c) show  $\Omega_d = 0, 0.5, 2$  with  $\Omega_c/\Gamma_2 = 0$ , which shows the transition from EIT to Autler-Townes splitting. Panels (d) to (f) show how increasing the coupling Rabi frequency ( $\Omega_c/\Gamma_2 = 0.25, 0.5, 2$ ) for a large dressing Rabi frequency ( $\Omega_d/\Gamma_2 = 2$ ) results in increasing electromagnetically induced absorption (EIA) at three-photon resonance [88, 89]. To create three-photon EIT a different set of detunings and Rabi frequencies must be found.

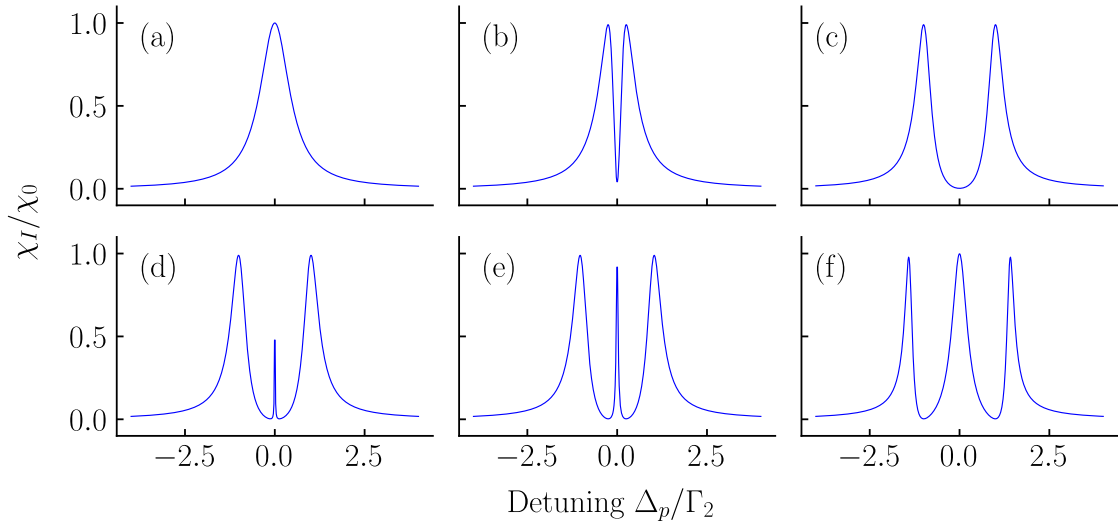


Figure 3.5: Four-level normalised imaginary weak probe susceptibility against normalised probe detuning. Panels (a) to (c) show  $\Omega_d = 0, 0.5, 2$  with  $\Omega_c/\Gamma_2 = 0$  and (d) to (f) show  $\Omega_c/\Gamma_2 = 0.25, 0.5, 2$  for  $\Omega_d = 2$ . The normalised decays are  $\Gamma_3/\Gamma_2 = 0.01$  and  $\Gamma_4/\Gamma_2 = 0.001$  throughout, and  $\Delta_d = \Delta_c = 0$ .

Four-level EIT is derived here by following Ref. [13], which assumes a weak probe and a strong dressing beam such that  $\Omega_d \gg \Omega_c \gg \Omega_p$ . This creates a middle step Autler-Townes splitting with eigenstates  $|\pm\rangle$  separated in frequency space by  $\Omega_d/(2\pi)$  for a sufficiently large  $\Omega_d$ . By creating a dressing beam bare state resonance through  $\Delta_d = 0$  in the limiting case of  $\Omega_p = \Omega_c$  and with  $\Delta_p = -\Delta_c = \pm\Omega_d/2$ , diagonalising the four-level Hamiltonian yields a dark state  $|D\rangle$  of

$$|D\rangle = \frac{|1\rangle - m(|2\rangle + |3\rangle) + |4\rangle}{\mathcal{N}}, \quad (3.12)$$

where  $\mathcal{N}$  is a normalisation factor and the mixing term  $m$  is

$$m = \frac{-\Omega_d + \sqrt{\Omega_d^2 + \Omega_c^2}}{\Omega_c}. \quad (3.13)$$

This mixing term  $m$  tends to zero as the dressing strength increases thereby making the dark state a superposition of the ground and Rydberg states,  $|D\rangle = (|1\rangle + |4\rangle)/\mathcal{N}$ . Therefore, for a strong dressing beam resonant with the bare atom transition  $|2\rangle \rightarrow |3\rangle$ , EIT is recovered under three-photon resonance but with the probe and coupling

beams tuned to one of the Autler-Townes split dressed states  $|\pm\rangle$ . This dressed basis is visualised in Fig. 3.6, where the probe and coupling beams have been drawn to be resonant on the  $|+\rangle$  state and the corresponding normalised weak probe imaginary susceptibility showing EIT is plotted on the right.

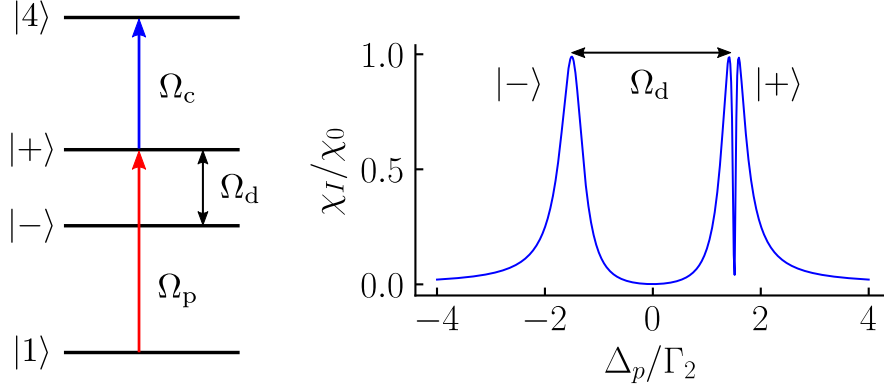


Figure 3.6: Left: the dressed state basis for  $\Omega_d \gg \Omega_c \gg \Omega_p$  with  $\Delta_d = 0$  and Autler-Townes split states  $|\pm\rangle$ , where the probe and coupling beams are tuned to  $|+\rangle$ . Right: the corresponding normalised weak probe imaginary susceptibility showing EIT with  $\Omega_d/\Gamma_2 = 3$ ,  $\Omega_c/\Gamma_2 = 0.25$ ,  $\Gamma_3/\Gamma_2 = 0.01$  and  $\Gamma_4/\Gamma_2 = 0.001$ .

Creating EIT through dressed state resonances also has the advantage of detuning the probe beam away from the  $D_1$  line resonance by  $\Delta_p = \pm\Omega_d/2$ . This reduces the absorption of the probe pulse as it propagates to the three-beam overlap region. Allowing a weaker incident probe pulse more closely replicates EIT and improves the efficiency of Rydberg polariton storage. If the Doppler-broadened width of an absorption lineshape is  $\Delta\omega_D = (\omega_0/c)\sqrt{k_B T/m}$ , then the probe absorption is greatly reduced if the detuning exceeds twice the Doppler width

$$\Omega_d > \frac{2\omega_0}{c} \sqrt{\frac{k_B T}{m}}. \quad (3.14)$$

For caesium's  $D_1$  line resonant frequency and mass [37] at room temperature, the dressing Rabi frequency must satisfy  $\Omega_d/(2\pi) > 300$  MHz. For hotter vapours and to further guarantee absorption reductions, the target value for future experiments in this thesis is set as  $\Omega_d/(2\pi) = 1$  GHz. This value will be recalled in design calculations in the next section.

### 3.2.3 STIRAP pulse timing diagram

Small dipole matrix elements between the lower and Rydberg levels results in small Rabi frequencies that must be compensated for with increased beam powers and/or reduced beam sizes. Alternatively, stimulated Raman adiabatic passage (STIRAP) can be used as a population transfer technique because it predicts a near-unity efficiency transfer between two atomic states [90].

Strong dressing maps the four-level system to a three-level dressed basis, so two-photon STIRAP [91] can be used to transfer ground state atoms to Rydberg levels. The eigenstates for a three-level ladder under two-photon resonance ( $\Delta_p + \Delta_c = 0$ ) are given back in Eqs. 2.16 where the zero eigenenergy STIRAP dark state is  $|v_0\rangle = (\Omega_c |1\rangle - \Omega_p |4\rangle) / \sqrt{\Omega_p^2 + \Omega_c^2}$  with a Rydberg state  $|4\rangle$ . The efficiency of STIRAP transfer tends to unity if the population is kept in the dark state during the transfer [92] and adiabaticity is recovered if [93]

$$\frac{\Omega_{p0}^2 + \Omega_{c0}^2}{\pi^2 \Gamma} \gg \frac{1}{T} \gg \gamma, \quad (3.15)$$

where  $(\Omega_{p,c})_0$  are the peak Rabi frequencies,  $\Gamma$  is the natural decay rate of the two middle dressed states,  $T$  is the pulse switching time and  $\gamma$  is the linewidth associated with the frequency difference of the probe and coupling beams.

Atoms are in  $|v_0\rangle = |1\rangle$  if  $\Omega_p = 0$  and  $\Omega_c \neq 0$  thereby requiring the coupling beam pulse to occur before the probe pulse. Thereafter  $\Omega_c$  is turned off and  $\Omega_p$  is switched on whilst maintaining the adiabaticity inequality resulting in  $|v_0\rangle \rightarrow |4\rangle$ . The Rydberg blockade described in Section 3.1.2 then prevents more than one excitation in the beam overlap region and the dark state polariton is stored. To retrieve the stored photon from the collective matter excitation [31],  $\Omega_c$  is turned back on to convert the polariton back to an optical excitation. Since dressed state STIRAP occurs in the presence of a constant and strong resonant  $\Omega_d$ , this allows the photon storage and retrieval scheme to be drawn in Fig. 3.7. The pulse widths,

rise times and amplitudes are not drawn to scale. The diagram is based on previous cold atom single-photon Rydberg level storage and photon counting experiments in Durham University [12, 94, 95].

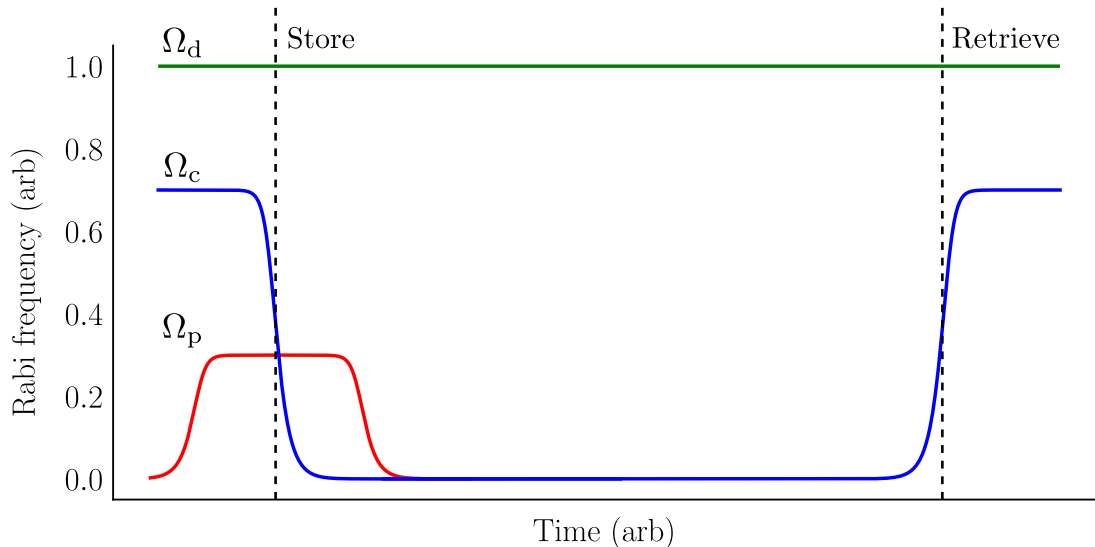


Figure 3.7: Dressed-state STIRAP pulse timing diagram for Rydberg polariton storage and retrieval. The probe photon (red) is stored as a dark state polariton as the control field (blue) is turned off. It is retrieved when the control field is turned back on. The strong dressing beam is on throughout (green line) and amplitudes, timings and pulse widths are not drawn to scale.

### 3.3 Custom Doppler-free cuvette

In this section the experimental reality of overlapping three focused beams at nonzero angles in a thermal vapour cell is considered. This thesis is based on previous work from Ref. [13] where three beams with  $1/e^2$  waists on the order of tens of microns were overlapped in a  $L = 2$  mm cylindrical caesium vapour cell. It was found that the focal distortion from focusing beams across the cell faces severely increased the complexity of beam overlapping. To combat such difficulties, a bespoke hexagonal vapour cell was designed and the calculations are presented here.

### 3.3.1 Focal distortion across planar interfaces

The motivation for designing a bespoke three-photon vapour cell arises from considering beam focusing across tilted planar interfaces. Figure 3.8 shows a lens at an arbitrary nonzero angle relative to a planar interface focusing a beam to a point in free space (black solid lines) and with the interface present (dashed lines). Each incident collimated ray is refracted by an amount that depends on its radial position on the lens' back focal plane. The angle of focusing  $\theta$  relative to the incident beam's optical axis satisfies  $\theta \leq \alpha$ , where the numerical aperture (NA) of the lens and the refractive index of the medium between the lens and the surface,  $n$ , define the acceptance angle through  $\text{NA} = n \sin \alpha$ .

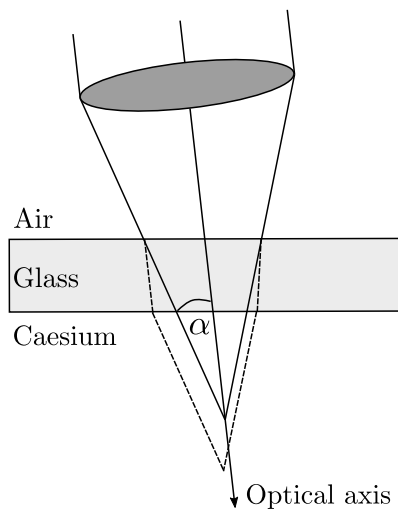


Figure 3.8: Visualising how a planar interface causes focal distortion for a non-normally incident beam. The solid black lines represent free-space focusing of paraxial rays and the dashes show the refracted paraxial rays.

The optical path differences of each ray due to the interface causes focal splitting through the astigmatism aberration [96]. To counter this, Ref. [13] designed mounted quartz plates that pre-aberrated the beam such that after focusing the total accumulated aberration was reduced. A more systematic methodology would be to pre-aberrate the beam using a liquid crystal spatial light modulator to apply a phase profile that recovers the free-space focus [97]. The accumulated aberration phase profile can be decomposed into the Zernike polynomial basis [98], which is

orthogonal over the unit circle and each mode can be adjusted independently. Profiling the beam in the presence of the cell cannot be done by simply placing a CCD camera in the beam path. Therefore the Zernike coefficients should be adjusted whilst maximising another measurable quantity such as single photon counts.

### 3.3.2 Cuvette design and fabrication

A cell design is presented where the incident beams see faces orthogonal to their optical axes thereby minimising the potential astigmatism. This is done by constructing a hexagon with faces that are orthogonal to the required Doppler-free angles arising from Eq. 3.6. A hexagon was chosen instead of a triangle because the exit face for each beam must also be orthogonal to the incident wave vector. Figure 3.9 shows the Doppler-free geometry in (a) and the resulting hexagon angles in (b).

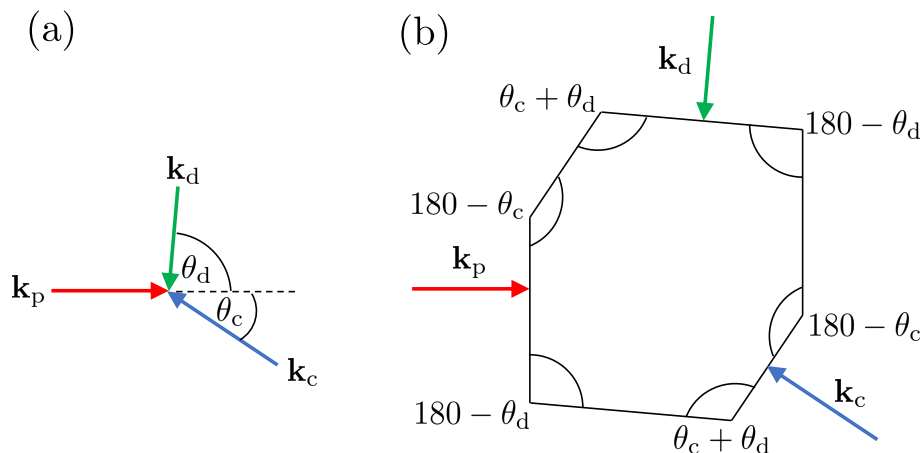


Figure 3.9: The three-photon Doppler-free cell design process. Panel (a): the Doppler-free geometry and (b): a hexagon with faces orthogonal to each beam.

Assuming an ideal Gaussian beam of wavelength  $\lambda$  with a  $1/e^2$  waist  $w_0$  focused by a lens of focal length  $f$  gives the diffraction-limited focal plane waist [99] as

$$w_f = \frac{f\lambda}{\pi w_0} . \quad (3.16)$$

For a target focal plane waist  $w_f$  at a wavelength  $\lambda$ , either the required focal length  $f$  can be calculated for an incident  $w_0$  or vice versa. Note that real diffraction-limited

aspherical lenses have focal lengths on the order of  $f = 17.5$  to  $20$  mm, and sub-centimetre thicknesses,  $t_{\text{lens}}$ . The cell wall thickness was chosen to be  $t_{\text{wall}} = 2$  mm for mechanical integrity and working distances, WD, between the lens and the cell faces should be at least a few millimetres to give component adjustment room.

A large Rydberg level  $n = 60$  was chosen giving a coupling wavelength of  $\lambda_c = 779.03$  nm. The target probe, dressing and coupling focal plane waists were chosen as  $w_{p, d, c} = 3, 4$  and  $6$   $\mu\text{m}$  to be smaller than the Rydberg blockade radius,  $R_B$ , at  $n \sim 60$  of  $R_B \sim 5$   $\mu\text{m}$ . Note that these design values do not claim to constitute optimal values for this three-beam single-photon scheme. For example, with pre-focussed beam waists of  $w_0 = 2$  mm for all three beams, the required focal lengths are given in Table 3.2. The corresponding Rayleigh lengths  $z_R$  are tens of microns, which makes the beam overlap very sensitive to focal shifts.

	Probe	Dressing	Coupling
$w_0(\text{mm})$	2	2	2
$w_f(\mu\text{m})$	3	4	6
$\lambda(\text{nm})$	894.6	1359.2	779.0
$z_R(\mu\text{m})$	31.6	37.0	145.2
$f(\text{mm})$	21.1	18.5	48.4

Table 3.2: Focal lengths for the probe, dressing and coupling beams given target focal plane waists  $w_f$  and incident waists  $w_0$  and a target Rydberg level  $n = 60$ .

The intersection volume of the two smallest beams can be approximated by assuming that the focusing hyperboloids remain as cylinders over the Rayleigh lengths. This gives an under-estimate of the actual interaction volume. For two cylinders with radii  $r_1 < r_2$  intersecting at an acute angle  $\beta$ , their analytic overlap volume [100] is

$$V = \frac{8}{\sin \beta} \int_0^{r_1} \sqrt{(r_1^2 - z^2)(r_2^2 - z^2)} dz . \quad (3.17)$$

Inserting  $r_1 = w_{0p}$ ,  $r_2 = w_{0d}$  and  $\beta = \theta_d$  yields  $V \approx 209.7$   $\mu\text{m}^3$ . By then setting  $V = 4\pi r^3/3$ , the equivalent sphere radius becomes  $r = 3.69$   $\mu\text{m}$ , which is well

within the probe Rayleigh range from Table 3.2 of  $z_R = 31.6 \mu\text{m}$ . Therefore, this intersecting cylinder argument is a good representation of the overlap volume that returns a radius less than the blockade radius at a Rydberg level  $n = 60$ .

The corresponding Doppler-free angles are  $\theta_d, \theta_c = 85.01^\circ$  and  $34.82^\circ$ , which creates near right-angles between the probe and dressing windows (see Fig. 3.9(b)). A design challenge then arises where the entry and exit probe faces have to be sufficiently overlapped to allow the emitted photon to see an orthogonal exit face. This is achieved by reducing the size of the coupling beam windows to bring the entry and exit probe faces closer together. However, this reduces the amount of coupling light entering the cell, so the whole cell must be scaled up in size. Following this argument, a hexagonal cell was designed with angles from Eq. 3.6 and dimensions shown in Fig. 3.10. The dimensions were chosen arbitrarily to give working distances of a few millimetres whilst accounting for the focal lengths in Table 3.2. Figure 3.10(a) shows the drawing and (b) shows a photo of the top face, where the near-right angle dressing and probe face joins are visible.

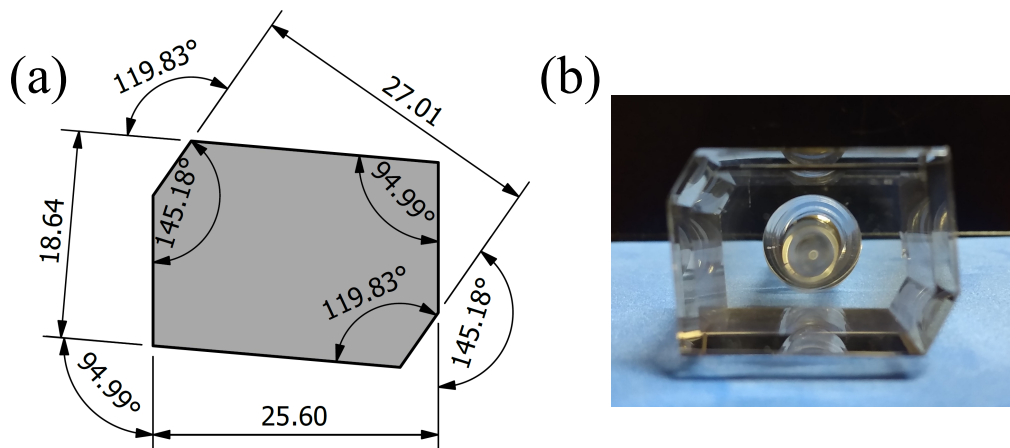


Figure 3.10: Top-down view of the hexagonal cell internal angles and external dimensions based on the parameters in Table 3.2. Drawing (a) and photo (b).

The cavity height and thickness are 20 mm and 2 mm, respectively. The cell was evacuated and filled by glass blowers on-site at Durham University's Department of Chemistry. The cell head was connected to the evacuation system via a cylindrical

glass flange with internal and external diameters of 6 and 11 mm and length 25 mm. Therefore a 15 mm length cylindrical stub was included in the cell design and the cell was fabricated by an external company. Figure 3.11 shows the head (24 mm), the stem (15 mm) and the glassblowers' flange ( $\sim 25$  mm). Labels (a) and (b) show caesium condensation on the cell windows and in the reservoir which can be removed by a heat gun. Further viewing angles of the cell are shown in Fig. 3.12 where the cell head wall thickness is more easily seen.

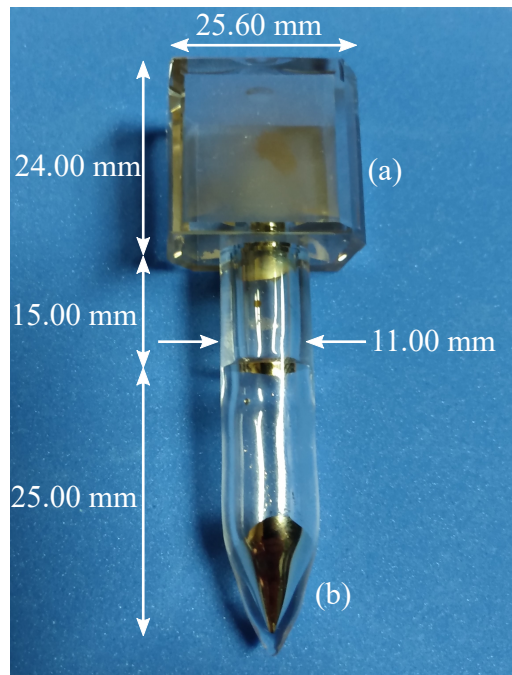


Figure 3.11: Three-photon cell dimensions where (a) and (b) show Cs condensation.

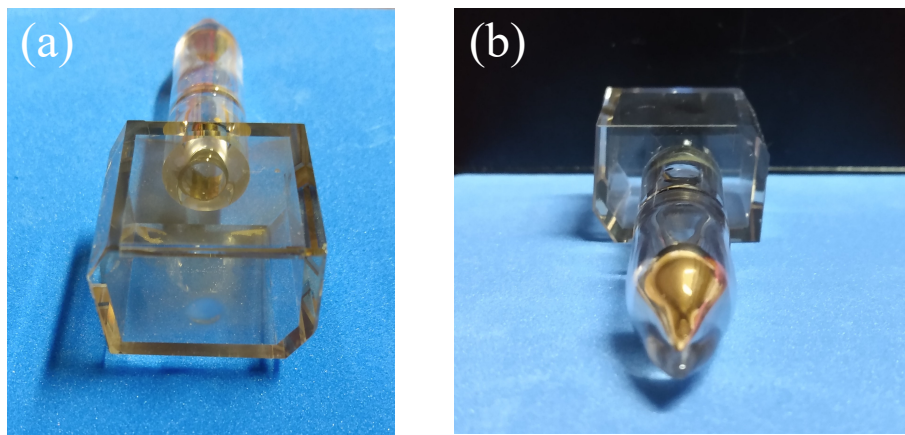


Figure 3.12: Top (a) and bottom (b) face views of the hexagonal caesium cell.

### 3.3.3 Simulating transmission and velocity selection

Given here are continuous wave (CW) and pulsed illumination simulations for the dressed system. The target Rydberg state is  $|60P_{1/2}\rangle$  and the example hyperfine transitions are  $|6S_{1/2}, F = 4\rangle \rightarrow |6P_{1/2}, F = 3\rangle \rightarrow |7S_{1/2}, F = 4\rangle \rightarrow |60P_{1/2}, F = 3\rangle$  corresponding to  $\theta_{d, c} = 85.00^\circ$  and  $34.82^\circ$  for a zero-wave vector. The dressed dark states  $|\pm\rangle$  require a probe detuning of  $\Delta_p = \pm\Omega_d/2$  and three-photon resonance coupling detunings of  $\Delta_c = \mp\Omega_d/2$ . All beams are assumed to drive  $\Delta m_F = 0$  transitions and the caesium temperature is  $T = 150^\circ\text{C}$ .

The detuned probe absorption only occurs in the beam overlap region, so the probe propagation length is approximated as twice the  $5\ \mu\text{m}$  blockade radius giving  $L \approx 10\ \mu\text{m}$ . Beams are approximated as being collimated with  $1/e^2$  waists of  $w_{p, d, c} = 3, 4$  and  $6\ \mu\text{m}$  from Table 3.2. Uniform intensity profiles are assumed with  $P_{p, d, c} = 1\ \text{pW}, 91\ \mu\text{W}$  and  $400\ \text{mW}$ . A weak probe is chosen and the coupling power corresponds to CW output powers available from common Ti:Sa laser systems. The dressing power gives the target dressed state splitting of  $\Omega_d/(2\pi) = 1\ \text{GHz}$  for  $w_d = 4\ \mu\text{m}$ . Hyperfine root mean square dipole matrix elements are calculated as

$$d = \sqrt{\sum_{m_{F_a}=-F_a}^{F_a} d^2(n_a, L_a, J_a, F_a, m_{F_a}, n_b, L_b, J_b, F_b, m_{F_b})}, \quad (3.18)$$

for the general hyperfine transition  $|n_a, L_a, J_a, F_a, m_{F_a}\rangle \rightarrow |n_b, L_b, J_b, F_b, m_{F_b}\rangle$  across all degenerate Zeeman sublevels.

The optical Bloch equations were solved using the method described in Appendix C. The Hamiltonian and decay matrices from Eqs. 3.9 and 3.10 include hyperfine structure and Doppler shifts in the diagonal element detunings. The probe and dressing beam Doppler shifts are  $-\mathbf{k}_p \cdot \mathbf{v}$  and  $-(\mathbf{k}_p + \mathbf{k}_d) \cdot \mathbf{v}$ , and the coupling Doppler shift is zero because  $\mathbf{k} = \mathbf{0}$ . A transit time broadening was included corresponding to the smallest of the beam waists,  $w_p$ , calculated using Eq. 2.29 to give  $\Gamma_{\text{tt}}/(2\pi) = 11.7\ \text{MHz}$ .

Figure 3.13 shows the CW steady-state OBE solution to  $\text{Im}\{\tilde{\rho}_{21}\}$  (a) and the normalised imaginary susceptibility (b) for the dressed state  $|-\rangle$  as colour maps against the 2D velocity  $(v_x, v_y)$  for three-photon resonance using the above parameters. The probe propagation direction is the x-axis. Velocity selection in the form of a locus of increasing magnitude coherence in negative  $v_y$  is mapped to a centralised region of susceptibilities in (b) where near-zero velocity classes contribute most greatly to the absorption coefficient, as is expected in EIT.

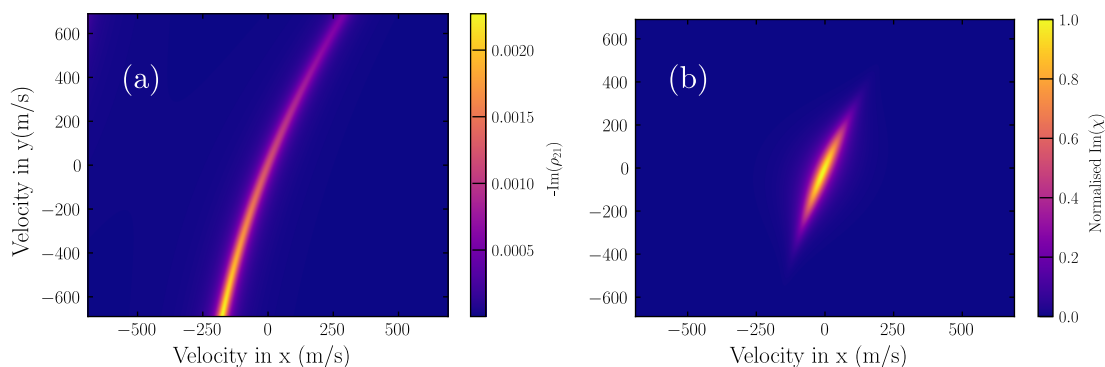


Figure 3.13: The imaginary coherence (a) and normalised imaginary susceptibility (b) for the dressed four-level system using parameters described above.

Shown in Fig. 3.14 is the corresponding Doppler-averaged transmission spectrum. The 1 GHz Autler-Townes splitting about the  $|6S_{1/2}, F = 4\rangle \rightarrow |6P_{1/2}, F = 3\rangle$  line centre is visible and the dark state EIT peak is seen in the left-hand dip. The  $|+\rangle$  state EIT peak would appear in the right-hand dip. Due to the very small hyperfine RMS coupling Rydberg dipole matrix element of  $d_c/(a_0e) = 1.22 \times 10^{-3}$  the EIT feature is very weak. For comparison, the probe and dressing transitions have much larger matrix elements of  $d_p/(a_0e) = 1.40$  and  $d_d/(a_0e) = 1.50$ . To increase the EIT strength for a more effective polariton storage, the atomic number density should be increased [31] and the already large coupling beam power and near-diffraction-limited focal radii could be increased and decreased, respectively.

Pulsed illumination is investigated by simulating dressed state STIRAP from Section 3.2.3. The target dressed state ( $|-\rangle$ ) and beam parameters remain the

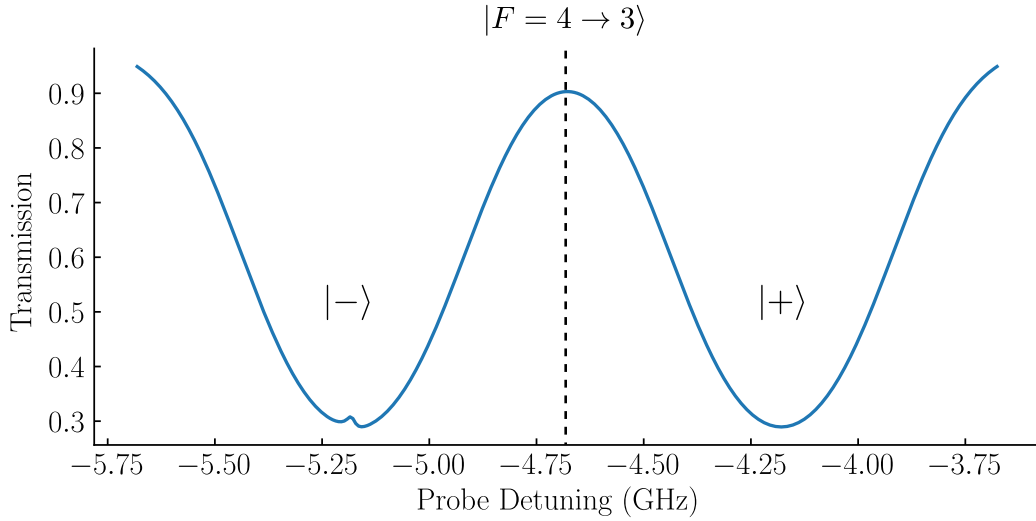


Figure 3.14: Doppler-averaged transmission of the colour map from Fig. 3.13(b).

same. A hyperbolic tangent pulse shape [31] gives an envelope of

$$\frac{2P(t)}{P_0} = \tanh\left(\frac{t - t_0}{w}\right) - \tanh\left(\frac{t - t_0 - T}{w}\right), \quad (3.19)$$

where the shape against time  $t$  with an offset  $t_0$ , characteristic width  $T$  and rise/fall time parameter  $w$  is normalised against peak power  $P_0$ . The pulse parameters in this simulation are  $t_0 = 5$  ns,  $T = 10$  ns,  $w = 0.45$  ns and  $(P_0)_{p, d, c} = 1$  pW, 91  $\mu$ W and 400 mW. The parameter  $w$  resulted in a rise and fall time of  $t_{\text{rise, fall}} = 1.04$  ns, which is shown to be experimentally achievable in a later section. The normalised probe and coupling pulse Rabi frequencies are given in Fig. 3.15(a) with the corresponding coherence against time in (b). The two pulses overlap temporally at their 50/50 point are in the presence of a constant dressing beam. The imaginary coherence follows the probe pulse.

Figure 3.16 shows the four level populations against time with the same pulse scheme present. The ground  $\rho_{11}$ , first  $\rho_{22}$  and second  $\rho_{33}$  excited state populations follow the probe pulse shape, where  $\rho_{11}$  decreases during illumination representing STIRAP to the Rydberg level. Populations  $\rho_{22}$  and  $\rho_{33}$  increase slightly representing non-unity STIRAP efficiency. The Rydberg population  $\rho_{44}$  reaches a maximum

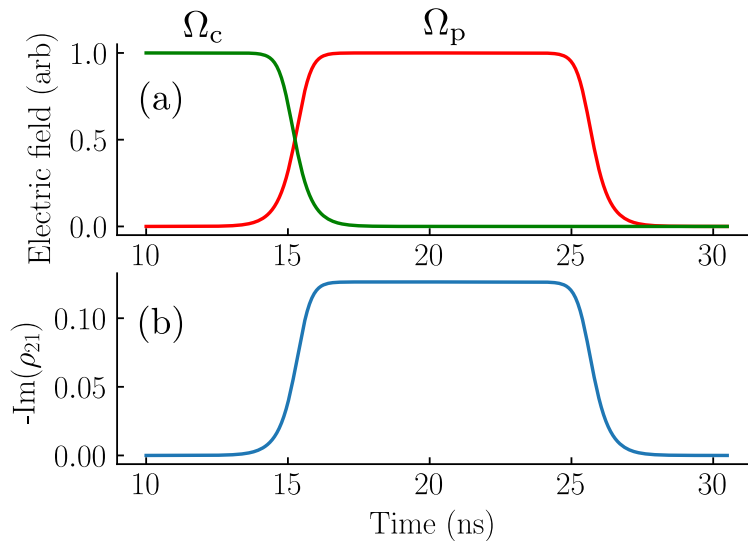


Figure 3.15: Dressed state STIRAP with normalised pulse amplitudes (a) and the corresponding imaginary coherence (b) for the parameters described above.

that is much smaller than the maximum of  $\rho_{22,33}$  which is explained by the weak EIT transmission spectrum feature from Fig. 3.14. Stronger EIT would yield a higher peak Rydberg population. However, the Rydberg population does not get maintained across the pulse exposure suggesting photon storage as a polariton across a window of a few nanoseconds. Additionally, the populations  $\rho_{22,33}$  should be near zero because STIRAP bypasses them when mapping ground state atoms to Rydberg levels.

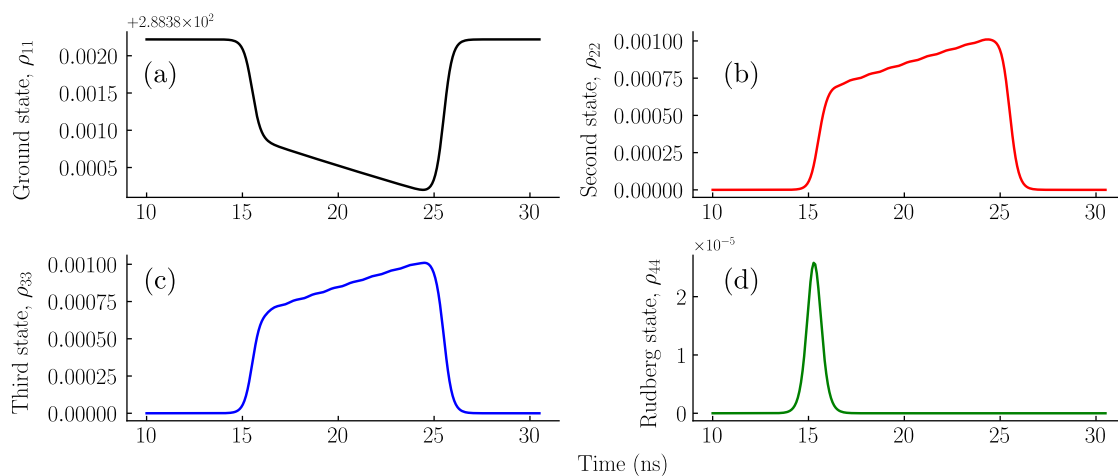


Figure 3.16: The four level populations with dressed state STIRAP for a target dressed dark state  $|-\rangle$ . Simulation parameters are found in the paragraphs above.

This pulsed simulation requires validation through a probe photon counting experiment where the polariton should be read out as an optical excitation. Different parameters should be investigated to explore the storage time limit. These are the time between  $\Omega_c$  turn off and turn on, the probe and coupling pulse switching time, and the repetition rate of the store/retrieve cycle. Successful future quantum technologies would operate as fast as the beam modulators, which could be tens or hundreds of megahertz for devices such as lithium niobate electro-optic modulators.

### 3.3.4 Knife edge probe beam waist data

Since the three-photon scheme relies on overlapping micrometre-scale beams inside a cell, it is important to consider how the 2 mm cell walls would affect the foci. A preliminary experiment was performed with an available  $f = 50$  mm plano-convex lens and a 2 mm mounted glass blank, where the beam focal plane waist was measured with and without the glass via knife edging (see Appendix B). The glass was placed approximately 25 mm from the lens' back face. A locus of Gaussian profile 895 nm probe beam waist sizes against the beam propagation axis was plotted in Fig. 3.17(a) without (red) and with the glass (blue). The loci should be hyperbolic [50] with limiting linear slopes, as is seen in panels (b) and (c).

The free-space data in (b) in red shows linear regions having different magnitude slopes of  $-13.1 \mu\text{m}/\text{mm}$  and  $8.44 \mu\text{m}/\text{mm}$  likely due to an aberrated beam. Fitting a hyperbola around the minimum datapoints was found to not be possible, so averaging the positions of the two lowest datapoints returned the minimum at approximately  $z = -4.51$  mm. The linear slopes in (c) are  $-13.8 \mu\text{m}/\text{mm}$  and  $16.2 \mu\text{m}/\text{mm}$  and panel (d) shows a successful hyperbolic fit to the data around the minimum approximated at  $z = -3.64$  mm. This gave a z-axis focal shift of  $\Delta z = 0.87$  mm, as well as a correction of the linear slopes. This correction is not explained in this thesis and requires more investigation. Since the proposed three-beam scheme requires high NA but shorter focal length diffraction-limited lenses, the focal shift is

likely to still be significant. This is essential to investigate in a future knife edging experiment because the Rayleigh lengths for the three micrometre-scale beams are on the order of tens of microns, as calculated in Table 3.2.

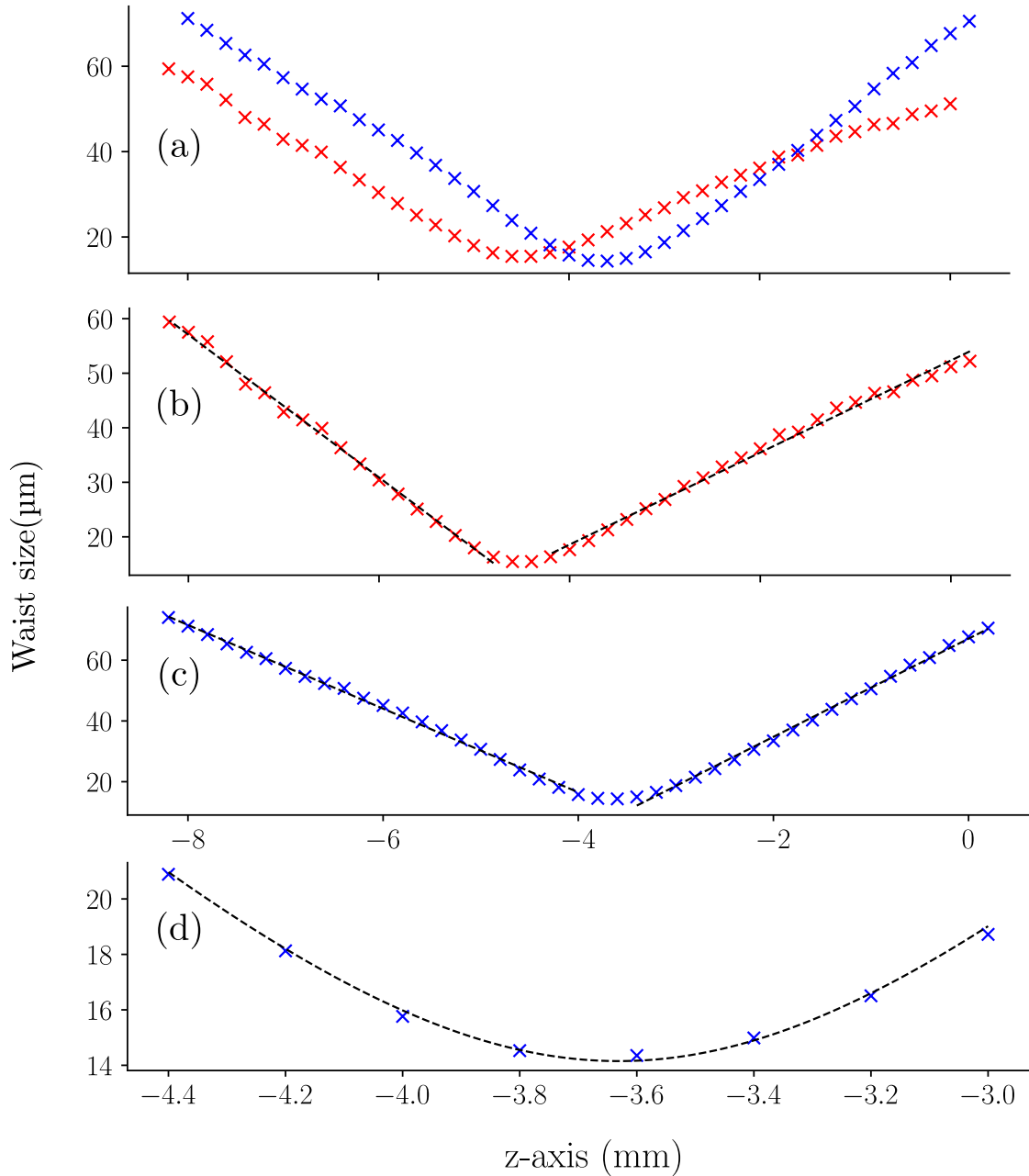


Figure 3.17: Beam waist against propagation distance for an 895 nm Gaussian beam focused with an  $f = 50$  mm plano-convex lens without (red) and with (blue) a 2 mm glass blank at approximately 25 mm from the lens' back face. Panel (a) is the data overlap, (b) and (c) are linear regressions on the data, and (d) is a hyperbolic fit to the data with glass.

## 3.4 Future experimental layout

The final section of this thesis proposes an experimental implementation of the single photon storage and emission scheme previously described in this chapter. It presents preliminary data for laser frequency stabilisation, probe beam amplitude modulation and suggests components for an optical layout.

### 3.4.1 Ground state polarisation spectroscopy data

Lasers experience frequency drifts that can exceed absorption linewidths due to noise sources such as temperature fluctuations, mechanical vibrations and quantum noise [101]. To frequency stabilise the 895 nm probe beam, a sub-Doppler pump-probe spectroscopy technique known as polarisation spectroscopy is investigated. It generates a steep slope dispersive error signal that is fed into a laser controller with a negative feedback PID loop [102]. By setting the target output frequency as the on-resonance zero crossing the feedback loop minimises the frequency difference. The laser frequency is then ‘locked’ to an atomic transition.

Polarisation spectroscopy requires a linearly polarised probe and a circularly polarised pump beam derived from the same laser [103]. The pump induces  $\sigma_{\pm}$  transitions, which creates a ground state population anisotropy through optical pumping leading to a birefringence in the propagation medium. When the probe field propagates through the birefringent medium, the probe’s circular basis components experience a phase shift and attenuation [104]. For light driving  $\sigma_{\pm}$  transitions the birefringent absorption coefficients and refractive indices are  $\alpha_{\pm}$  and  $n_{\pm}$  with the corresponding wavevectors being  $k_{\pm} = (\omega/c)n_{\pm}$ .

Splitting the probe beam into horizontal and vertical  $x$  and  $y$  components using a polarising beam splitter and taking their difference returns a signal of

$$I_y - I_x = I_0 e^{-\alpha L} \cos\left(\phi + \frac{\omega L}{c} \Delta n\right). \quad (3.20)$$

Here,  $\phi$  is the plane of polarisation of the probe relative to the global  $x$ -axis before propagation through the medium. The value  $\alpha = (\alpha_+ + \alpha_-)/2$  is the average absorption coefficient and  $\Delta n = n_+ - n_-$  is the refractive index birefringence. Additionally, propagation through the birefringent medium further rotates the probe's plane of polarisation by an angle  $\Phi = \omega L \Delta n / c$ . If  $\Phi$  is small and the input plane of polarisation is set as  $\phi = \pi/4$  to maximise the signal  $I_y - I_x$  [104], then for a transition natural linewidth  $\Gamma$ , a resonant difference in absorption coefficients  $\Delta\alpha_0$  and a laser detuning  $\Delta$ , the resulting signal is

$$I_y - I_x = I_0 e^{-\alpha L} L \Delta\alpha_0 \frac{2\Delta/\Gamma}{1 + (2\Delta/\Gamma)^2} . \quad (3.21)$$

This profile is proportional to the derivative of a Lorentzian arising from the Kramers Krönig relation linking  $\Delta n$  and  $\Delta\alpha$ . The steep slope arising from the Lorentzian natural width  $\Gamma$  allows for the feedback loop to respond quickly to frequency drifts.

To implement polarisation spectroscopy, the experimental setup in Fig. 3.18 is presented. The bottom branch represents the linearly polarised probe propagating through a caesium bulk cell from left to right. It is incident on the very right-hand PBS where two photodiodes ( $\text{PD}_\pm$ ) return the dispersive differencing signal  $I_y - I_x$ . The signal is fed back into the laser controller driving the 895 nm laser. A stronger probe counter-propagates in the bottom cell at a nonzero crossing angle with the use of an edge mirror, where a  $\lambda/4$  waveplate creates the necessary circular polarisation. The middle and upper branches are for time to frequency mapping and time axis calibration - see Appendix A.

Experimental data was gathered for the caesium  $D_1$  line (see Fig. 2.8) at room temperature in a  $L = 75$  mm bulk cell, which was shielded against stray magnetic fields with a mu-metal shield. Figure 3.19 shows the evolution of the  $D_1$  line polarisation spectroscopy spectrum with varying probe powers of  $P_p = 5, 14, 22, 35$   $\mu\text{W}$  in panels (a) to (d). The pump power was constant at  $P_{\text{pump}} = 270$   $\mu\text{W}$  and both

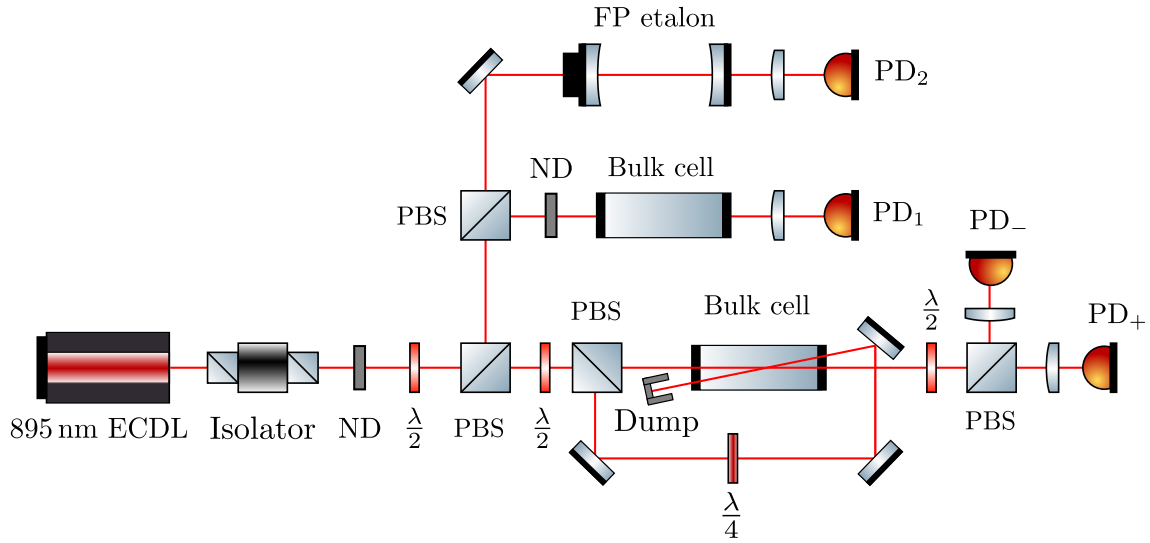


Figure 3.18: Experimental setup for polarisation spectroscopy. A circularly polarised pump counter-propagates against a linearly polarised probe beam, which is incident on the positive and negative inputs of a differencing photodiode. The etalon and bulk cell are for time axis calibration and frequency mapping.

beams were collimated with  $1/e^2$  waists of approximately  $w_0 = 1$  mm. The traces were normalised to the strongest feature corresponding to the  $F = 4 \rightarrow F' = 3$  transition. All four features were isolated from each other due to the large hyperfine ground  $6S_{1/2}$  and excited  $6P_{1/2}$  state splittings of 9.19 GHz and 1.17 GHz.

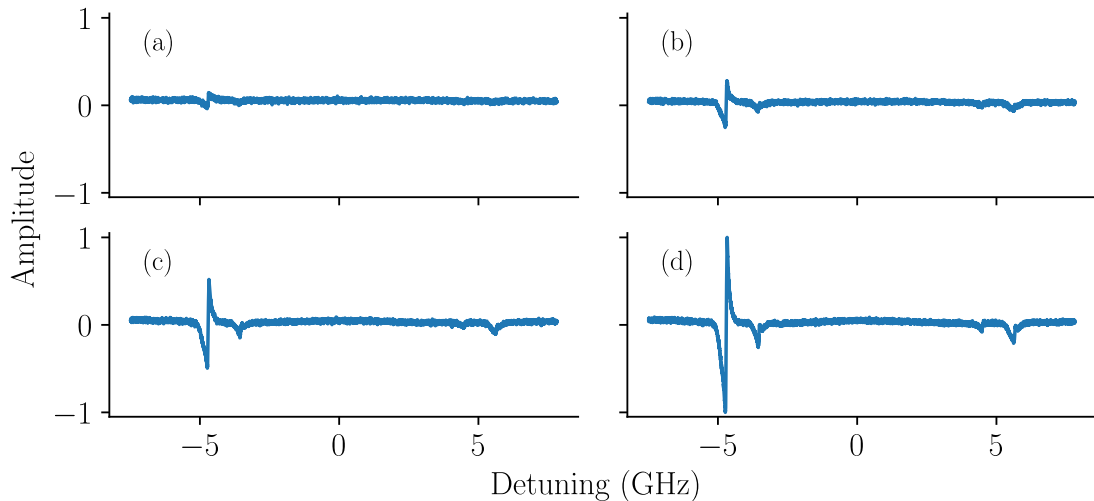


Figure 3.19: Polarisation spectroscopy signals for the caesium  $D_1$  line. A room temperature  $L = 75$  mm vapour cell was used with a pump power of  $P_{\text{pump}} = 270 \mu\text{W}$  and probe powers of  $P_{\text{probe}} = 5, 14, 22, 35 \mu\text{W}$  in panels (a) to (d).

### 3.4.2 Probe beam amplitude EOM pulse data

Recall that the probe beam must be made weak and become pulsed for storage as a dark state polariton. After frequency stabilising the laser, a specific device needs to be chosen to amplitude modulate the beam based on a set of pulse shape requirements and practical operating features.

Some key pulse requirements include rise time, fall time, repetition rate and maximum continuous wave input power. Ideally, the rise and fall times would be zero thereby giving perfect rectangular pulses but realistic signal generators driving the modulators need to be considered. Signal generators have a trade-off between their rise time  $t_R$  and their three decibel (3dB) half power bandwidth  $f_{3dB}$  due to capacitances that must be charged and discharged in their internal circuitry. Approximating the generator's transfer function as a low-pass filter of resistance  $R$  and capacitance  $C$  with a decay constant  $\tau = RC$  gives an approximate 10/90 rise time of  $t_R = \ln(9)/(2\pi f_{3dB})$  [105].

In this thesis, pulse data from an amplitude electro-optic modulator (EOM) from Jenoptik is presented because it has sub-nanosecond rise times for the near-infrared wavelengths of 500 ps. However, its maximum CW input is 30 mW, but this is not a problem because the probe should be weak. Moreover, devices like Pockels cells and acousto-optic modulators (AOMs) allow for larger input powers but have slower switching times (10s of nanoseconds for AOMs) or half-wave Voltages on the order of 100 V to 1000 V (for Pockels cells) requiring bulky Voltage amplifiers.

The amplitude EOM is a lithium niobate crystal fibre-coupled device designed for  $895 \pm 5$  nm. It has an extinction ratio of 30 dB and a half-wave Voltage of 2.54 V. It was driven using a Tektronix AWG 4162 with a switching time of 800 ns and the modulated light was focused onto an AC-coupled EOT ET-2030A amplified silicon detector with  $t_{\text{rise/fall}} < 500$  ps and a high sensitivity of more than  $400 \text{ VW}^{-1}$ . A LeCroy oscilloscope was used to display and capture the pulse data. Additionally, a half waveplate and polarising beam splitter cube were placed before the EOM input

fibre. This pair maximises the input coupled power and linearly polarises the input light by aligning the input beam’s plane of polarisation with the fibre’s polarisation maintaining axis and by cleaning the polarisation of the light by discarding the reflected beam from the cube.

Figure 3.20 shows the shortest pulse created with the Tektronix signal generator given in amplitude normalised data. The trailing edge shows some ringing, which is likely from the finite discharge times of capacitances in the photodetector. An artefact-free pulse shape would be measured by photon counting.

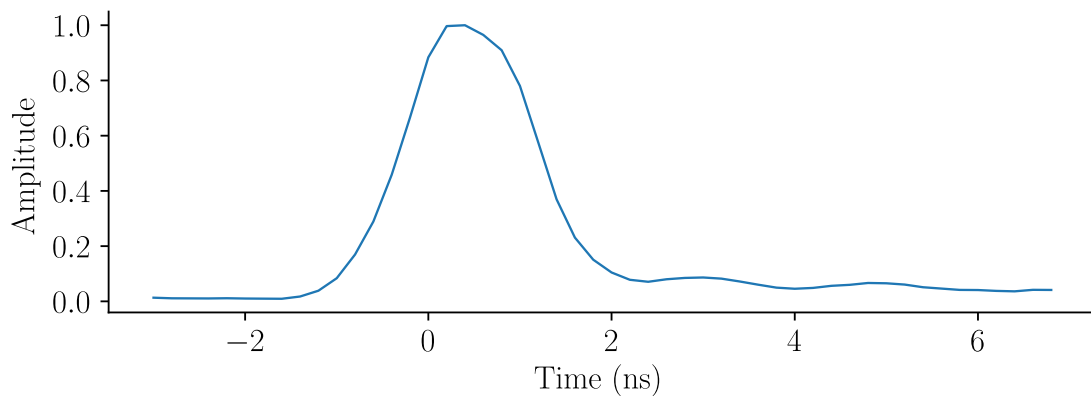


Figure 3.20: Normalised probe pulse amplitude from an EOT AC-coupled photodiode against time. A lithium niobate Jenoptik amplitude EOM driven by a Tektronix AWG 4162 generated 800 ps rise and fall times.

### 3.4.3 Experimental layout suggestions

The closing subsection of this chapter discusses potential implementations of the three-beam single photon emitter scheme described throughout. It considers the probe, dressing and Rydberg coupling beams systematically and includes the hexagonal caesium cell described previously.

#### Laser frequency stabilisation

As a reminder, the presence of a strong dressing beam maps the four-level system to a three-level dressed system. Additionally, the middle dark states were shown

to be detuned from the  $D_1$  line by  $\pm\Omega_d/2$  and a target dressing Rabi frequency of  $\Omega_d/(2\pi) = 1$  GHz was chosen to shift the dressed state resonance out of the  $D_1$  absorption line. This requires the probe to be detuned by  $\pm\Omega_d/2$  depending on the chosen middle dark state  $|\pm\rangle$ , but the dressing beam is tuned to the  $6P_{1/2} \rightarrow 7S_{1/2}$  transition. The dressing beam therefore can be frequency stabilised from a frequency stabilised probe beam using excited state polarisation spectroscopy [106]. This is where a stabilised probe beam and additional polarisation spectroscopy hardware is used to stabilise the dressing beam, as was explained for the probe in the previous subsection.

Further consideration needs to be applied to choose a frequency stabilisation scheme for the Rydberg beam. Options include a simpler scheme such as Rydberg EIT locking [107] through to master-slave digital controller based scanning transfer cavity lock schemes [108]. An upper bound on the linewidth of the locked laser should be evaluated along with the long-term stability through the Allan deviation.

### **Amplitude modulation**

Since the dressing beam power will need to be on the order of hundreds of milli Watts to create  $\Omega_d/(2\pi) = 1$  GHz with micrometre-scale foci, then EOMs cannot be used. Alternatively, an AOM can be used to switch the dressing beam on and off on a timescale of tens of nanoseconds that exceeds the nanosecond-scale probe and Rydberg pulses. To pulse the Rydberg beam, an appropriate EOM should be identified, purchased and implemented.

### **Probe and coupling beam frequency offsets**

The dressed scheme requires a probe and coupling offsets of half the dressed state Rabi frequency, which is set to 500 MHz. The probe beam can then be shifted by  $\Omega_d/(2\pi) = 500$  MHz using an acousto-optic modulator, as was done in [13]. A suitable device needs to be chosen for the coupling beam.

# Chapter 4

## Conclusion

This thesis presented the initial design, simulations and experiments towards deterministic single-photon emission a caesium thermal vapour excited to Rydberg levels. Realising quantum technologies is an open problem and a deterministic thermal vapour implementation of a single photon source based on linear optics is a very attractive end goal.

### 4.1 Summary of key results

Chapter one presented electromagnetically induced transparency (EIT) as a means to transfer atoms to an upper state population in a ladder scheme. EIT was investigated in a low-lying three-level ladder in a caesium thermal vapour, where a derived model and experiment agreed to a qualitative level.

Chapter two explored EIT in a four-level ladder scheme where optical excitations can be mapped to collective states known as Rydberg polaritons. A single-photon storage and emission scheme was presented for a three-beam Doppler-free illumination scheme. A custom hexagonal cuvette was also designed to minimise the astigmatism aberration that arises from focusing beams across tilted planar interfaces. Simulations of continuous wave and pulsed EIT were given for realistic parameters in the four-level scheme. Calculations were performed for required beam powers and

focal plane waists. Finally, laser frequency stabilisation via polarisation spectroscopy and amplitude modulation using an electro optic modulator were experimentally investigated. Polarisation spectroscopy demonstrated stabilisation error signals with steep slopes and zero crossings with a simple experimental layout, and the probe beam modulation rise times of around one nanosecond suggest a place for lithium niobate EOMs in a final experimental layout.

## 4.2 Outlook

The next stage for this project is to build and test the single photon emitter scheme, which can be broken down as follows. Firstly, using the parameters calculated in this thesis a three-beam overlap with micrometre-scale focal plane waists in the presence of the hexagonal Doppler-free caesium vapour cell should be performed. This quality of overlap could be measured and optimised by tracking changes in the CW probe transmission, where a Rydberg EIT peak should occur. Secondly, probe beam photon counting should be performed with dressed state ground-to-Rydberg STIRAP. This allows for checking the polariton retrieval and storage efficiencies. Finally, given a working system, the  $g^{(2)}(\tau)$  second-order correlation coefficient should be calculated to measure the nature of the retrieved photons. A near-zero  $g^{(2)}(\tau = 0)$  dip is expected for a high quality single-photon source.

# Appendix A

## Data linearisation and normalisation

The process of time axis linearisation and transmission normalisation is presented here for the caesium D<sub>1</sub> line. Firstly, nonlinearities in the probe laser scan prevent a linear time to frequency conversion arising from temperature fluctuations, mechanical vibrations and the finite laser linewidth. Secondly, as the piezoelectric transducer (PZT) disc in the ECDL rotates to perform the scan, the amount of output coupled light from the ECDL reduces, which gives a scan amplitude background. Overall, the time axis must be calibrated and the scanning background must be removed.

Temporal calibration requires an etalon spectrum (Fig. A.1) where peaks are known to be constantly separated in frequency by the free spectral range (FSR). Temporally, the peaks will have non-constant spacings. By plotting the peak number against time, a linear regression can be made to approximate the linear peak spacing in time (Fig. A.2 (a)). By subtracting the linear function from the points, a deviation from linearity can be plotted at each instance in time (Fig. A.2 (b)). Thereafter, interpolating and subtracting the deviation polynomial from the time axis returns the calibrated, linearised time.

The frequency dependence of the transmission background is seen in Fig. A.3. A

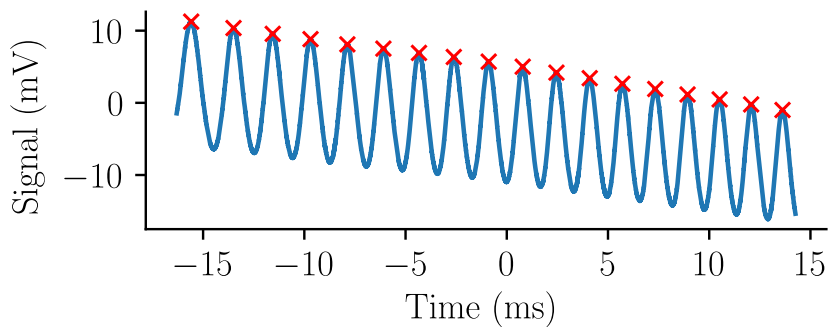


Figure A.1: The low-finesse etalon used for time axis calibration in this thesis. Peaks are marked in red crosses.

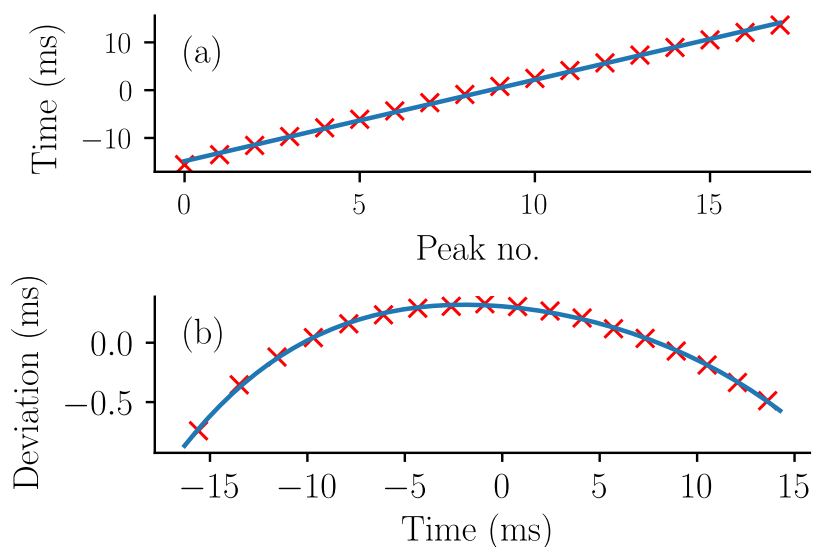


Figure A.2: Plotting the etalon peaks against the peak number (a) and the temporal deviation from a linear regression (b).

low-order polynomial is then fitted to the unity transmission regions (red) and the background slope is approximated. By dividing the trace by the background, the spectrum becomes normalised. Finally, the normalised spectrum and its four minima (Fig. A.4 (a)) are plotted against time. A regression between the four peaks' known frequency detunings and temporal occurrences allows a time to frequency detuning mapping (Fig. A.4 (b)).

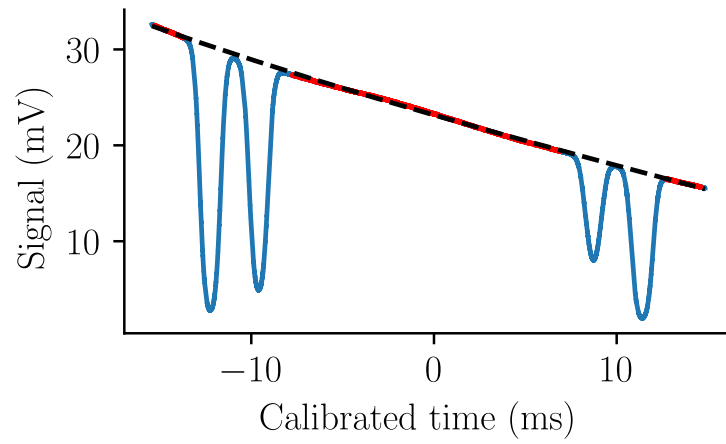


Figure A.3: Caesium  $D_1$  data (blue) with unity transmission regions (red) and a background polynomial (black).

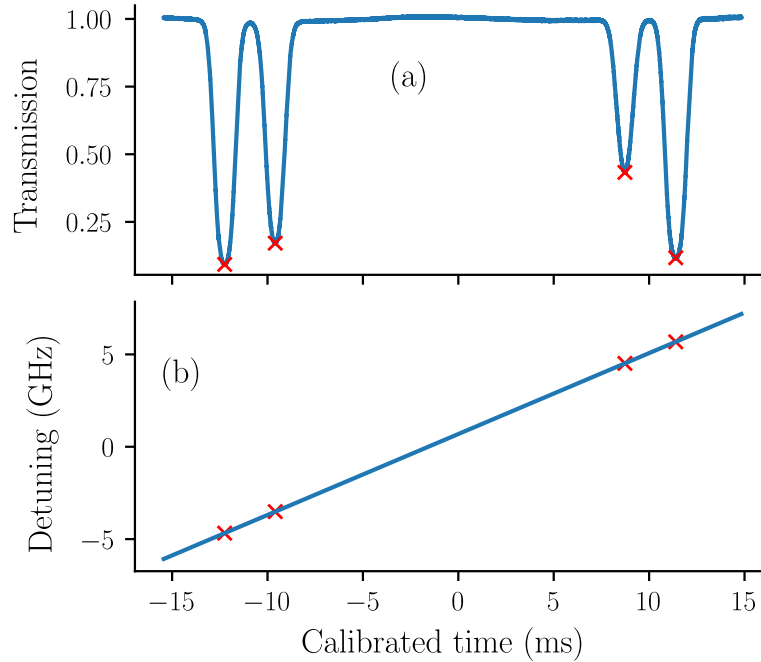


Figure A.4: Normalised  $D_1$  transmission with red markers indicating minima in time (a) and the regression on the four minima to map time to frequency detuning (b).

# Appendix B

## Knife edge beam waist extraction

This appendix explains the process of measuring beam waists using knife edges. Assume that the beam waist propagates along the z-axis and that a knife edge (razor blade) is translated laterally into the beam path along the x-axis. The beam locus waist  $w_0$  is located at  $(z_0, x_0)$  and is assumed to follow a hyperbolic profile dependent on  $z$  as

$$w(z) = w_0 \sqrt{1 + \left(\frac{z}{z_R}\right)^2}, \quad (\text{B.1})$$

with a Rayleigh length  $z_R = \pi w_0^2/\lambda$ . For elliptical beams translating the beam along the x-axis extracts  $w_x$  and along the y-axis returns  $w_y$ .

Figure B.1 shows the scenario where a blade is translated along the x-axis thereby blocking the beam from minus infinity to position  $x$ . Since the y-axis transmission is unaffected (assuming a perfectly sharp edge without any tilt), the power incident on the photodetector follows the integral of the Gaussian beam intensity distribution as the error function through

$$P_{\text{detector}}(z, x) = P_{\text{background}} + \frac{P_{\text{max}}}{2} \left( 1 - \operatorname{erf} \left( \frac{\sqrt{2}(x - x_0)}{w(z)} \right) \right). \quad (\text{B.2})$$

When  $x$  is at minus infinity corresponding to the absence of a blade then the detected power is the maximum power plus the background I.e.  $P_{\text{detector}} = P_{\text{background}} + P_{\text{max}}$ .

Normalising the detected power by the maximum and fitting error functions against  $x$  at a given  $z$  then allows the waist to be extracted and plotted against  $z$ . Fitting a hyperbola to this waist locus then returns the focal plane waist,  $w_0$ .

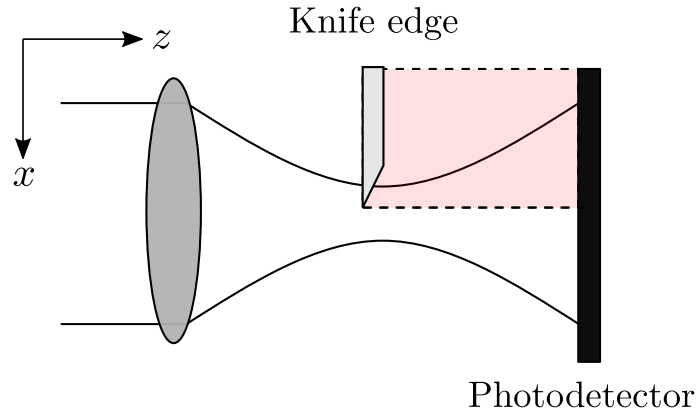


Figure B.1: Schematic showing a knife edge translated laterally into a beam path. The blocked beam is highlighted in pink and is not detected on the photodetector.

# Appendix C

## Solving the optical Bloch equations

In this thesis, the optical Bloch equations are solved by re-casting the problem to a vector equation by using the Choi-Jamiolkowski isomorphism to create a matrix superoperator [109]. An alternative is the Runge-Kutta method [110], but the presented method is cleaner due to employing linear algebra.

Firstly, the density matrix  $\tilde{\rho}$  for an  $N$ -level system is reshaped into a column vector  $\tilde{\boldsymbol{\rho}}$  with dimensions  $N^2 \times 1$ . Secondly, the isomorphism replaces  $[\tilde{H}, \tilde{\rho}]$  with  $(\tilde{H} \otimes \mathbb{I} - \mathbb{I} \otimes \tilde{H}^\dagger) \tilde{\boldsymbol{\rho}}$ , where  $\mathbb{I}$  is the identity matrix. Thirdly, the decay matrix is replaced by an augmented matrix  $L$  of dimensions  $N^2 \times N^2$  multiplying the column vector  $\tilde{\boldsymbol{\rho}}$  through  $\mathcal{L}(\tilde{\rho}) \rightarrow L \tilde{\boldsymbol{\rho}}$ . The system of equations is then written more compactly as

$$\frac{d\tilde{\boldsymbol{\rho}}}{dt} = M \tilde{\boldsymbol{\rho}}, \quad (\text{C.1})$$

where the  $N^2 \times N^2$  superoperator  $M$  is used

$$M = \tilde{H} \otimes \mathbb{I} - \mathbb{I} \otimes \tilde{H}^\dagger + L. \quad (\text{C.2})$$

The linear algebra solution is  $\tilde{\boldsymbol{\rho}}(t) = e^{Mt} \tilde{\boldsymbol{\rho}}(t=0)$  and an eigenvector decomposition

of  $M = W \text{diag}\{e^{\lambda_i t}\}W^{-1}$  returns a cleaner expression to evaluate yielding

$$\tilde{\boldsymbol{\rho}}(t) = W \text{diag}\{e^{\lambda_i t}\}W^{-1}\tilde{\boldsymbol{\rho}}(0) . \quad (\text{C.3})$$

The eigenvectors of  $M$  are stacked in the matrix  $W$  and the corresponding  $N^2$  eigenvalues  $\lambda_i$  are placed in the diagonal matrix  $\text{diag}\{e^{\lambda_i t}\}$ .

The coherence  $\tilde{\rho}_{21}$  is needed for calculating absorption spectra and the following presents a quicker way of finding this value when atoms are initialised in the ground state,  $\boldsymbol{\rho}(0) = (1, 0, \dots, 0)^T$ . For a  $N$ -level system the coherence  $\tilde{\rho}_{21}$  is the  $(N + 1)^{\text{th}}$  value of  $\tilde{\boldsymbol{\rho}}(t)$ . Manipulating matrix elements then reveals that the coherence can be calculated from the following matrix elements

$$\tilde{\rho}_{21} = (W)_{N+1,N+1} (W^{-1})_{N+1,1} e^{\lambda_{N+1} t} , \quad (\text{C.4})$$

which reduces the number of computationally expensive matrix multiplications. This is important when looping over thousands of velocities during Doppler averaging.

# Bibliography

- [1] D. Jaksch, J. I. Cirac, and P. Zoller. Fast quantum gates for neutral atoms. *Phys. Rev. Lett.*, 85(10):2208–2211, 2000.
- [2] L. Isenhower, E. Urban, X. L. Zhang, A. T. Gill, T. Henage, T. A. Johnson, T. G. Walker, and M. Saffman. Demonstration of a neutral atom controlled-NOT quantum gate. *Phys. Rev. Lett.*, 104:010503, 2010.
- [3] C. S. Adams, J. D. Pritchard, and J. P. Schaffer. Rydberg atom quantum technologies. *J. Phys. B: At. Mol. Opt. Phys.*, 53:1–13, 2020.
- [4] O. Firstenberg, C. S. Adams, and S. Hofferberth. Nonlinear quantum optics mediated by Rydberg interactions. *J. Phys. B: At. Mol. Opt. Phys.*, 49:152003, 2016.
- [5] H. Busche, P. Huillery, S. W. Ball, T. Ilieva, M. P. A. Jones, and C. S. Adams. Contactless nonlinear optics mediated by long-range Rydberg interactions. *Nat. Phys.*, 13:655–670, 2017.
- [6] J. Hidary. *Quantum computing : an applied approach*. Springer, 2019.
- [7] T. Ladd, F. Jelezko, R. Laflamme, Y. Nakamura, C. Monroe, and J. L. O’Brien. Quantum computers. *Nature*, 464:45–53, 2010.
- [8] E. Knill, R. Laflamme, and G. J. Milburn. A scheme for efficient quantum computation with linear optics. *Nature*, 409:46–52, 2001.
- [9] P. Kok, W. J. Munro, K. Nemoto, T. C. Ralph, J. P. Dowling, and G. J. Milburn. Linear optical quantum computing with photonic qubits. *Rev. Mod. Phys.*, 79:135–174, 2007.

- [10] Y. O. Dudin and A. Kuzmich. Strongly interacting Rydberg excitations of a cold atomic gas. *Science*, 336:887–889, 2012.
- [11] M. Fleischhauer and M. D. Lukin. Dark state polaritons in electromagnetically induced transparency. *Phys. Rev. Lett.*, 84:5094–5097, 2000.
- [12] D. Maxwell, D. J. Szwer, D. Paredes-Barato, H. Busche, J. D. Pritchard, A. Gauguet, K. J. Weatherill, M. P. A. Jones, and C. S. Adams. Storage and control of optical photons using Rydberg polaritons. *Phys. Rev. Lett.*, 110:103001, 2013.
- [13] N. Sibalic, J. M. Kondo, C. S. Adams, and K. J. Weatherill. Dressed-state electromagnetically induced transparency for light storage in uniform-phase spin waves. *Phys. Rev. A*, 94:033840, 2016.
- [14] M. D. Eisaman, J. Fan, A. Migdall, and S. V. Polyakov. Invited review article: single-photon sources and detectors. *Rev. Sci. Instrum.*, 82:071101, 2011.
- [15] J. McKeever, A. Boca, A. D. Boozer, R. Miller, J. R. Buck, A. Kuzmich, and H. J. Kimble. Deterministic generation of single photons from one atom trapped in a cavity. *Science*, 303:1992–1994, 2004.
- [16] M. Keller, B. Lange, K. Hayasaka, W. Lange, and H. Walther. Continuous generation of single photons with controlled waveform in an ion-trap cavity system. *Nature*, 431:1075–1078, 2004.
- [17] C. Brunel, B. Lounis, P. Tamarat, and M. Orrit. Triggered source of single photons based on controlled single molecule fluorescence. *Phys. Rev. Lett.*, 83:2722–2725, 1999.
- [18] C. Kurtsiefer, S. Mayer, P. Zarda, and H. Weinfurter. Stable solid-state source of single photons. *Phys. Rev. Lett.*, 85:290–293, 2000.
- [19] E. Neu, D. Steinmetz, J. R. Moeller, S. Gsell, M. Fischer, M. Schreck, and C. Becher. Single photon emission from silicon-vacancy colour centres in chemical vapour deposition nano-diamonds on iridium. *New J. Phys.*, 13:025012, 2011.

- [20] P. Michler, A. Kiraz, C. Becher, W. V. Schoenfeld, P. M. Petroff, L. Zhang, E. Hu, and A. Imamoglu. A quantum dot single-photon turnstile device. *Science*, 290:2282–2285, 2000.
- [21] A. J. Bennett, D. C. Unitt, P. Atkinson, D. A. Ritchie, and A. J. Shields. High performance single photon sources from photolithographically defined pillar microcavities. *Opt. Express*, 13:50–55, 2005.
- [22] C. W. Chou, S. V. Polyakov, A. Kuzmich, and H. J. Kimble. Single-photon generation from stored excitation in an atomic ensemble. *Phys. Rev. Lett.*, 92:213601, 2004.
- [23] M. M. Müller, A. Kölle, R. Löw, T. Pfau., T. Calarco, and S. Montangero. Room-temperature rydberg single-photon source. *Phys. Rev. A*, 87:053412, 2013.
- [24] F. Ripka, H. Kübler, R. Löw, and T. Pfau. A room-temperature single-photon source based on strongly interacting Rydberg atoms. *Science*, 362:446–449, 2018.
- [25] Y. H. Kim and W. P. Grice. Measurement of the spectral properties of the two-photon state generated via type II spontaneous parametric downconversion. *Opt. Lett.*, 30:908–910, 2005.
- [26] E. A. Goldschmidt, M. D. Eisaman, J. Fan, S. V. Polyakov, and A. Migdall. Spectrally bright and broad fiber-based heralded single-photon source. *Phys. Rev. A*, 78:013844, 2008.
- [27] R. S. Matthew. *Single-photon generation via four-wave mixing in a thermal rubidium vapour at a high magnetic field*. PhD thesis, University of Durham, 2021. Available at Durham E-Theses online: <http://etheses.dur.ac.uk/13903/>.
- [28] B. Lounis and M. Orrit. Single-photon sources. *Rep. Prog. Phys.*, 68:1129–1179, 2005.
- [29] G. Solomon P. Senellart and A. White. High-performance semiconductor quantum-dot single-photon sources. *Nat. Nanotech.*, 12:1026–1039, 2017.

- [30] N. Tomm et al. A bright and fast source of coherent single photons. *Nat. Nanotech.*, 16:399–403, 2021.
- [31] M. D. Lukin, M. Fleischhauer, R. Cote, L. M. Duan, D. Jaksch, J. I. Cirac, and P. Zoller. Dipole blockade and quantum information processing in mesoscopic atomic ensembles. *Phys. Rev. Lett.*, 87:037901, 2001.
- [32] E. Urban, T. A. Johnson, T. Henage, L. Isenhower, D. D. Yavuz, T. G. Walker, and M. Saffman. Observation of Rydberg blockade between two atoms. *Nature Phys*, 5:110–114, 2009.
- [33] F. Ripka, Y. H. Chen, R. Löw, and T. Pfau. Rydberg polaritons in a thermal vapour. *Phys. Rev. A*, 93:053429, 2016.
- [34] T. Cutler, W. Hamlyn, J. Renger, Whittaker K, D. Pizzey, I. G. Hughes, V. Sandoghdar, and C. S. Adams. Nanostructured alkali-metal vapor cells. *Phys. Rev. A*, 14:034054, 2020.
- [35] J. G. Speight. *Environmental organic chemistry for engineers*. Elsevier, 2017.
- [36] R. K. Sinnott. *Chemical engineering design (4th ed.)*. Elsevier, 2017.
- [37] D. A. Steck. Cesium D line data. <http://steck.us/alkalidata>. Revision 2.2.1, 21 November 2019.
- [38] P. Hertz. Über den gegenseitigen durchschnittlichen Abstand von Punkten, die mit bekannter mittlerer Dichte im Räume angeordnet sind. *Mathematische Annalen*, 67:387–398, 1909.
- [39] D. Suter. *The physics of laser-atom interactions*. CUP, 1997.
- [40] G. Grynberg, A. Aspect, and C. Fabre. *Introduction to quantum optics: from the semi-classical approach to quantized light*. CUP, 2010.
- [41] C. Cohen-Tannoudji, J. Dupont-Roc, and G. Grynberg. *Atom-photon interactions: basic processes and applications*. Wiley-VCH, 2004.
- [42] C. J. Foot. *Atomic physics*. OUP, 2013.

- [43] K. Fujii. Introduction to the rotating wave approximation (RWA): two coherent oscillations. *J. Mod. Phys.*, 8:2042–2058, 2017.
- [44] G. W. Ford and R. F. O’Connell. The rotating wave approximation (RWA) of quantum optics: serious defect. *Physica A*, 243(3):377–381, 1997.
- [45] M. A. Nielsen and I. L. Chuang. *Quantum computation and quantum information*. CUP, 2010.
- [46] G. Lindblad. On the generators of quantum dynamical semigroups. *Commun. Math. Phys.*, 48:119–130, 1976.
- [47] R. Loudon. *The quantum theory of light*. OUP, 2010.
- [48] E. Hecht. *Optics: Fifth Edition*. Pearson Education Limited, Harlow, England, 2017.
- [49] B. Sherlock and I. G. Hughes. How weak is a weak probe in laser spectroscopy? *Am. J. Phys.*, 77(2):111–115, 2009.
- [50] CVI. Melles-Griot. Gaussian beam optics. Technical Report Vol. 2, Issue 1, Donald A. Glaser Advanced Laboratory, University of California, Berkeley, 2009.
- [51] K.-J Boller, A. Imamoglu, and S. E. Harris. Observation of electromagnetically induced transparency. *Phys. Rev. Lett.*, 66(20):2593–2596, 1991.
- [52] M. Xiao, Y. Li, S. Jin, and J. Gea-Banacloche. Measurement of dispersive properties of electromagnetically induced transparency in rubidium atoms. *Phys. Rev. Lett.*, 74(5):666–669, 1995.
- [53] S. E. Harris. Electromagnetically induced transparency. *Physics today*, 50(7):36–42, 1997.
- [54] M. Fleischhauer, A. Imamoglu, and J. Marangos. Electromagnetically induced transparency: Optics in coherent media. *Rev. Mod. Phys.*, 77:633–673, 2005.

- [55] J. Gea-Banacloche, Y. Li, S. Jin, and M. Xiao. Electromagnetically induced transparency in ladder-type inhomogeneously broadened media: Theory and experiment. *Phys. Rev. A*, 51:576–584, 1995.
- [56] P. M. Anisimov, J. P. Dowling, and B. C. Sanders. Objectively discerning Autler-Townes splitting from electromagnetically induced transparency. *Phys. Rev. Lett.*, 107:163604, 2011.
- [57] S. J. Blundell and K. M. Blundell. *Concepts in thermal physics*. OUP, 2010.
- [58] P. Siddons, C. S Adams, C. Ge, and I. G. Hughes. Absolute absorption on rubidium D lines: comparison between theory and experiment. *J. Phys. B: At. Mol. Opt. Phys.*, 41:1–10, 2008.
- [59] A. Urvoy, C. Carr, C. S. Adams, K. J. Weatherill, and R. Löw. Optical coherences and wavelength mismatch in ladder systems. *J. Phys. B: At. Mol. Opt. Phys.*, 46:245001, 2013.
- [60] G. K. Woodgate. *Elementary atomic structure*. OUP, 1983.
- [61] H. A. Bethe and E. E. Salpeter. *Quantum mechanics of one- and two-electron atoms*. Plenum Publishing Corporation, 1977.
- [62] D. M. Brink and G. R. Satchler. *Angular momentum*. OUP, 1968.
- [63] N. Šibalić, J. D. Pritchard, C. S. Adams, and K. J. Weatherill. ARC: An open-source library for calculating properties of alkali Rydberg atoms. *Comp. Phys. Comm.*, 220:319–331, 2017.
- [64] V. Gerginov, K. Calkins, C. E. Tanner, J. J. McFerran, S. Diddams, A. Bartels, and L. Hollberg. Optical frequency measurements of  $6s^2S_{1/2} - 6p^2P_{1/2}$  ( $D_1$ ) transitions in  $^{133}\text{Cs}$  and their impact on the fine-structure constant. *Phys. Rev. A*, 73:032504, 2006.
- [65] T. Udem, J. Reichert, R. Holzwarth, and T. W. Hänsch. Absolute optical frequency measurement of the caesium  $d_1$  line with a mode-locked laser. *Phys. Rev. Lett.*, 82:3568–3571, 1999.

- [66] M. Zentile, J. Keaveney, L. Weller, D. J. Whiting, C. S Adams, and I. G. Hughes. ElecSus: A program to calculate the electric susceptibility of an atomic ensemble. *Comp. Phys. Comm.*, 189:162–174, 2015.
- [67] J. Keaveney, C. S. Adams, and I. G. Hughes. ElecSus: Extension to arbitrary geometry magneto-optics. *Comp. Phys. Comm.*, 224:311–324, 2018.
- [68] S. G. Johnson. Faddeeva W function implementation. <http://ab-initio.mit.edu/Faddeeva>, 2012.
- [69] A. L. Fymat. Jones’s matrix representation of optical instruments.1: beam splitters. *Appl. Opt.*, 10(11):2499–2505, 1971.
- [70] E. Collet. *Field Guide to Polarization*. SPIE Press, 2005.
- [71] D. Smith and I. G. Hughes. The role of hyperfine pumping in multilevel systems exhibiting saturated absorption. *Am. J. Phys.*, 72(5):631–637, 2004.
- [72] A. Kortyna, N. A. Masluk, and T. Bragdon. Measurement of the  $6d^2D_j$  hyperfine structure of cesium using resonant two-photon sub-doppler spectroscopy. *Phys. Rev. A*, 74:022503, 2006.
- [73] T. J. Chen et al. Absolute frequency of cesium  $6S_{1/2}$ – $6D_{3/2}$  hyperfine transition with a precision to nuclear magnetic octupole interaction. *Opt. Lett.*, 43(9):1954–1957, 2018.
- [74] T. Ohtsuka, N. Nishimiya, T. Fukuda, and M. Suzuki. Doppler-free two-photon spectroscopy of  $6S_{1/2}$ – $6D_{3/2,5/2}$  transition in cesium. *J. Phys. Soc. Jpn*, 74:2487, 2005.
- [75] H. S. Moon and H.-R. Noh. Resonant two-photon absorption and electromagnetically induced transparency in open ladder-type atomic system. *Opt. Exp.*, 21:7447–7455, 2013.
- [76] M. Tanasittikosol. *Rydberg dark states in external fields*. PhD thesis, University of Durham, 2011.

- [77] S. D. Badger, I. G. Hughes, and C. S. Adams. Hyperfine effects in electromagnetically induced transparency. *J. Phys. B: At. Mol. Opt. Phys.*, 34:L749, 2001.
- [78] J. Huennekens, R. K. Namiotka, J. Sagle, Z. J. Jabbour, and M. Allegrini. Thermalization of velocity-selected excited-state populations by resonance exchange collisions and radiation trapping. *Phys. Rev. A*, 51:4472, 1995.
- [79] H.-R. Noh and H. S. Moon. Transmittance signal in real ladder-type atoms. *Phys. Rev. A*, 85:033817, 2012.
- [80] I. G. Hughes and T. P. A. Hase. *Measurements and their uncertainties: a practical guide to modern error analysis*. OUP, 2010.
- [81] T. W. Gallagher. *Rydberg atoms*. CUP, 1994.
- [82] T. W. Gallagher. Rydberg atoms. *Rep. Prog. Phys.*, 51:143–188, 1988.
- [83] D. Comparat and P. Pillet. Dipole blockade in a cold Rydberg atomic sample. *J. Opt. Soc. Am. B*, 27(6):A208–A232, 2010.
- [84] M. Fleischhauer and M. D. Lukin. Quantum memory for photons: dark-state polaritons. *Phys. Rev. A*, 65:022314, 2002.
- [85] M. Saffman and T. G. Walker. Creating single-atom and single-photon sources from entangled atomic ensembles. *Phys. Rev. A*, 66:065403, 2002.
- [86] C.-J. Lorenzen and K. Niemax. Quantum defects of the  $n^2 P_{1/2,3/2}$  levels in  $^{39}\text{K}$  I and  $^{85}\text{Rb}$  I. *Physica Scripta*, 27:300–305, 1983.
- [87] A. Browaeys, D. Barredo, and T. Lahaye. Experimental investigations of dipole–dipole interactions between a few Rydberg atoms. *J. Phys. B: At. Mol. Opt. Phys.*, 49:152001, 2016.
- [88] M. G. Bason, A. K. Mohapatra, K. J. Weatherill, and C. S. Adams. Narrow absorptive resonances in a four-level atomic system. *J. Phys. B: At. Mol. Opt. Phys.*, 42:075503, 2009.

- [89] J. M. Kondo, N. Šibalić, A. Guttridge, C. G. Wade, N. R. De Melo, C. S. Adams, and K. J. Weatherill. Observation of interference effects via four-photon excitation of highly excited Rydberg states in thermal cesium vapor. *Opt. Lett.*, 40:5570–5573, 2015.
- [90] K. Bergmann, H. Theuer, and B. W. Shore. Coherent population transfer among quantum states of atoms and molecules. *Rev. Mod. Phys.*, 70:1003–1025, 1998.
- [91] K. Bergmann, N. V. Vitanov, and B. W. Shore. Coherent population transfer among quantum states of atoms and molecules. *J. Chem. Phys.*, 142:170901, 2015.
- [92] L. P. Yatsenko, V. I. Romanenko, B. W. Shore, and K. Bergmann. Stimulated Raman adiabatic passage with partially coherent laser fields. *Phys. Rev. A.*, 65:043409, 2002.
- [93] K. Aikawa, D. Akamatsu, J. Kobayashi, M. Ueda, T. Kishimoto, and S. Inouye. Toward the production of quantum degenerate bosonic polar molecules,  $^{41}\text{K}$   $^{87}\text{Rb}$ . *New J. Phys.*, 11:055035, 2009.
- [94] Y. Jiao, N. L. R. Spong, O. D. W. Hughes, C. So, T. Ilieva, K. J. Weatherill, and C. S. Adams. Single-photon stored-light Ramsey interferometry using Rydberg polaritons. *Opt. Lett.*, 45:5888–5891, 2020.
- [95] N. L. R. Spong, Y. Jiao, O. D. W. Hughes, K. J. Weatherill, I. Lesanovsky, and C. S. Adams. Collectively encoded rydberg qubit. *Phys. Rev. Lett.*, 127:063604, 2021.
- [96] R. J. Knoll. Zernike polynomials and atmospheric turbulence. *J. Opt. Soc. Am.*, 66:207–211, 1976.
- [97] M. A. A. Neil, M. J. Booth, and T. Wilson. Closed-loop aberration correction by use of a modal Zernike wave-front sensor. *Opt. Lett.*, 25:1083–1085, 2000.
- [98] R. Tyson. *Principles of adaptive optics*. Elsevier, 1991.

- [99] C. S. Adams and I. G. Hughes. *Optics f2f: from Fourier to Fresnel*. OUP, 2019.
- [100] J. H. Hubbell. Common volume of two intersecting cylinders. *J. Res. Nat. Bur. Stand.-C: Eng. and Instrum.*, 69C:139–143, 1965.
- [101] S. Hooker and C. Webb. *Laser Physics*. OUP, 2010.
- [102] W. Nagourney. *Quantum electronics for atomic physics and telecommunication*. OUP, 2014.
- [103] C. Wieman and T. W. Hänsch. Doppler-free laser polarization spectroscopy. *Phys. Rev. Lett.*, 36(20):1170–1173, 1976.
- [104] C. P. Pearman, C. S. Adams, S. G. Cox, P. F. Griffin, D. A. Smith, and I. G. Hughes. Polarization spectroscopy of a closed atomic transition: applications to laser frequency locking. *J. Phys. B: At. Mol. Opt. Phys.*, 35:5141–5151, 2002.
- [105] P. Horowitz and W. Hill. *The art of electronics*. CUP, 2015.
- [106] C. Carr, C. S. Adams, and K. J. Weatherill. Polarization spectroscopy of an excited state transition. *Opt. Lett.*, 37:118–120, 2012.
- [107] Y. Jiao, J. Li, L. Wang, H. Zhang, L. Zhang, J. Zhao, and S. Jia. Laser frequency locking based on Rydberg electromagnetically induced transparency. *Chin. Phys. B*, 25:053201, 2016.
- [108] S. Subhankar, A. Restelli, Y. Wang, S. L. Rolston, and J. V. Porto. Microcontroller based scanning transfer cavity lock for long-term laser frequency stabilization. *Rev. Sci. Instrum.*, 90:043115, 2019.
- [109] M. Jiang, S. Luo, and S. Fu. Channel-state duality. *Phys. Rev. A*, 87:022310, 2013.
- [110] D. Manzano. A short introduction to the Lindblad master equation. *AIP Adv.*, 10:025106, 2020.